



## Topology optimization for compliance and contact pressure distribution in structural problems with friction

Kristiansen, Hansotto; Poullos, Konstantinos; Aage, Niels

*Published in:*  
Computer Methods in Applied Mechanics and Engineering

*Link to article, DOI:*  
[10.1016/j.cma.2020.112915](https://doi.org/10.1016/j.cma.2020.112915)

*Publication date:*  
2020

*Document Version*  
Peer reviewed version

[Link back to DTU Orbit](#)

*Citation (APA):*  
Kristiansen, H., Poullos, K., & Aage, N. (2020). Topology optimization for compliance and contact pressure distribution in structural problems with friction. *Computer Methods in Applied Mechanics and Engineering*, 364, Article 112915. <https://doi.org/10.1016/j.cma.2020.112915>

---

### General rights

Copyright and moral rights for the publications made accessible in the public portal are retained by the authors and/or other copyright owners and it is a condition of accessing publications that users recognise and abide by the legal requirements associated with these rights.

- Users may download and print one copy of any publication from the public portal for the purpose of private study or research.
- You may not further distribute the material or use it for any profit-making activity or commercial gain
- You may freely distribute the URL identifying the publication in the public portal

If you believe that this document breaches copyright please contact us providing details, and we will remove access to the work immediately and investigate your claim.

# Topology optimization for compliance and contact pressure distribution in structural problems with friction

Hansotto Kristiansen<sup>1,☆</sup>, Konstantinos Poullos<sup>1</sup>, Niels Aage<sup>1,2</sup>

<sup>1</sup>*Department of Mechanical Engineering, Solid Mechanics, Technical University of Denmark, Nils Koppels Alle, Building 404, 2800 Kongens Lyngby, Denmark*

<sup>2</sup>*Centre for Acoustic-Mechanical Micro Systems, Technical University of Denmark, 2800 Kongens Lyngby, Denmark*

---

## Abstract

This paper concerns density-based topology optimization of linear elastic contact problems, aiming to present robust and practically realizable designs for different objective functions. First we revisit a compliance minimization with frictionless contact problem from the literature and present crisp solid-void designs, based on the so-called modified robust topology optimization formulation. An adaptation of this problem to frictional contact is then solved for various friction coefficients and it is checked that the optimization algorithm indeed exploits the presence of friction for lowering the objective further. Secondly, we propose and demonstrate the use of a  $p$ -norm based objective function to control the distribution and variation of contact pressure, on an a priori unknown area of contact, between a body of unknown topology and an obstacle. To have control over the contact pressure, a Lagrange multiplier based contact formulation is used within a coupled Newton solution, for imposing impenetrability, friction, and the corresponding complementarity conditions. The adjoint method is employed for deriving consistent design sensitivities for the mixed formulation involving both displacements and contact Lagrange multipliers. Through a series of numerical examples, it is demonstrated how an even distribution of contact pressure and crisp solid-void designs can be obtained for problems with and without friction.

**Keywords:** topology optimization, unilateral contact, friction, contact pressure optimization

**2018 MSC:** XX-XX, XX-XX

---

---

<sup>☆</sup>Corresponding author. Email: Hakris@mek.dtu.dk

## 1. Introduction

Over the last couple of decades, the method of density based topology optimization [1] has successfully been applied to a large number of research fields such as solid mechanics [2], fluid mechanics [3, 4] and acoustics [5, 6]. A wealth of problems have been solved by this method, but many still remain unsolved. One class of such relatively little studied problems can be found at the junction with frictional contact mechanics. The available works in this area are mainly attributed to three pioneers, Klarbring, Strömberg and Hilding, who together have successfully applied shape, size and topology optimization methods to the class of unilateral contact problems throughout the years [7, 8, 9, 10, 11, 12, 13].

Models for structural optimization with unilateral contact can in general be categorized depending on whether they deal with compliance or contact force minimization. Moreover, they can be categorized according to the different types of design variables considered, including initial gap, truss member thickness or material density. Especially in the latter case, it is important to distinguish between pure solid-void designs and variable sheet thickness designs, i.e. design with intermediate density values. The present work focuses on contact pressure optimization with a density based design space and an enforcement of pure solid-void designs, where the latter is obtained using morphological filters, i.e. the robust formulation from [14]. We remark that other approaches for reaching pure solid-void design exists, e.g. by penalization as done in [15] or the single realization projection filter as done in [16], but that the robust formulation is chosen since this also provides control of minimum feature sizes rendering the optimized designs insensitive to over- and under-etching.

Regarding contact force optimization, in 1992, Klarbring proposed a method for optimizing the shape of an obstacle to achieve uniformly distributed contact forces [17]. For that specific problem a uniform contact force distribution could be achieved indirectly by minimization of a potential energy objective. The design variables were the size of the initial gaps between the rigid obstacle and a prescribed elastic body, whereas in the current work, we would like to optimize the topology of the structure itself. A relevant, in that respect, study is the one by Hilding et al. from 1999, in which one seeks to design a truss structure that minimizes the maximum unilateral contact force in a frictionless setting [7]. In that work, a non-smooth max-type objective function was considered, while we apply a  $p$ -norm based objective function instead.

When it comes to density based topology optimization methods, relatively few publications deal with the presence of contact and even fewer include friction. In the majority of the cases, the objective is compliance minimization. A few early papers [18, 19, 20, 21] address compliance minimization with a frictionless unilateral contact condition and they all solve approximately the same benchmark problem on a square domain with fixed support at its top and partial contact at its bottom. The problem is also featured in the review paper by Hilding, Klarbring and Petersson [22] from 1999. The reported solutions for this benchmark problem are interesting as a conceptual demonstration of the effect of a unilateral contact condition. Nevertheless, these designs are

in general not practically realizable, as the density (or thickness) field varies continuously from zero to one. Although compliance minimization is not the main focus of the present work, we use the opportunity to revisit this problem solving it with modern topology optimization methods and we report new  
50 pure solid-void solutions for various material constraints and load intensities. Moreover, we investigate the effect of including friction to this problem and we report designs that outperform designs optimized in the frictionless setting. More recent works in density based topology optimization of compliance under unilateral contact conditions include the aforementioned papers by Strömberg  
55 and Klarbring [9, 12] as well as the ones by Desmorat [23] and Andrade-Campos et al. [24], which all assume a frictionless condition. An extension of the frictionless case to large deformations has also been proposed by Luo et al. [25] in 2016, whereas the effect of sliding Coulomb friction in the context of compliance minimization was considered in [13].

60 One major concern regarding frictional problems, especially in the context of optimization, is the load path dependence and non-uniqueness of frictional forces. As a conservative solution to this problem, Hilding and Klarbring have proposed the likely state approach [26], which allows to account for frictional forces to the degree that these are necessary for restricting rigid body motion,  
65 while it reduces to the frictionless case for statically constrained structures. Without underestimating the importance of load path dependence in many practical problems, especially for loads with non-monotonic or non-proportional components, in the present work we choose to work with simple examples where the sliding direction can be approximated based on a single load increment. An  
70 extension of the proposed approach to time-dependent and dynamic problems is part of a future work by the authors.

Another work worth mentioning is the one by Lawry and Maute [27] which introduced a level-set based topology optimization framework for the design of  
75 two-component structures in cases where frictionless sliding contact and separation along the interfaces can occur. Maximization of the average normal stress on the Dirichlet boundary of the embedded component, led to stiff anchor designs between the two components with barb-type features forming the contact interface. This work is particularly interesting because it deals with contact between two elastically deformable bodies, while the contact interfaces considered  
80 in many other works, including the present one, are between an elastic body and a rigid obstacle. Nevertheless, the optimization in [27] does not involve the contact pressure at the interface as part of the objective function, as the current work does.

Considering now pressure optimization of contact problems, to the authors’  
85 best knowledge, applications of density based topology optimization with frictional contact and a contact pressure based objective function, have not yet been reported in the available literature. In those cases from the aforementioned literature where contact forces are in the objective, the optimization either refers to discrete structures or to the shape of a rigid obstacle. On the  
90 other hand, all cases employing a density based description of the topology are either directly or indirectly aiming at some sort of compliance minimization. In

this paper, building upon the existing literature, we propose an objective function that controls directly the contact pressure distribution by simultaneously minimizing the average and the variation of contact pressure on an a priori unknown contact area. The proposed objective function is smooth with one free  
95 parameter corresponding to the  $p$ -norm exponent  $q$ .

The proposed approach is to some degree related to previous works in structural optimization such as the aforementioned papers [17, 7] and the truss size optimization method by Klarbring et al. [28], from 1995. These works aim at  
100 a favorable distribution of contact pressure by either modifying the initial gap geometry, e.g. by performing shape optimization of the rigid obstacle, or by size optimization of a truss structure. The novelty of the proposed approach consists in applying modern density based topology optimization techniques, combined with a new pressure based objective function, for achieving constant  
105 contact pressure distributions while also accounting for Coulomb friction. The frictional test case investigated in this context is one where a fixed velocity is prescribed to the obstacle, corresponding to a steady state response. Steady state problems with Coulomb friction are only a limited subclass of problems observed in the real world, where friction acting opposite to motion will often  
110 lead to transient conditions. However, the chosen example is still well suited for demonstrating the applicability of the proposed objective function.

The paper is organized in six sections. Section 2 presents the numerical setup, introduces the concept of a gap function and describes the employed unilateral frictional contact formulation. Section 3 presents and describes the  
115 compliance objective and the proposed pressure objective function and Section 4 defines the topology optimization problem, including the adjoint sensitivity analysis. In Section 5 we present three test problems. The first test problem is the aforementioned compliance minimization benchmark and the two other test problems are used to demonstrate the proposed pressure based  
120 objective function. Finally, Section 6 summarizes all substantial findings.

## 2. Numerical setup

To keep the model presentation simple, plane stress linearized isotropic elasticity is considered throughout the present work, discretized with bi-linear four node quadrilateral finite elements. Please note, that the presented work does  
125 not make any underlying assumptions on isotropy nor any specific choice of elements until the numerical examples. The displacements of a selected set of finite element nodes are additionally unilaterally constrained by a rigid restricting boundary. The frictional unilateral contact formulation used in this work is based on the augmented Lagrangian approach proposed by Alart and  
130 Curnier [29], with the actual implementation being closer to the one described in [30], although adapted to a nodal enforcement of the contact conditions. We remark that using an elastic-rigid contact formulation is chosen for the sake of simplicity. Extending the framework to an elastic-elastic contact is straightforward - and applying topology optimization to such problem would be relatively  
135 straightforward as long as the interface elements are prescribed as solid. The

real complexity comes with including self-contact or design structures without well-defined boundaries, in which case the normal vectors may not be well-defined, and this would be complex even in an elastic-rigid setting. However, if self-contact is possible in an elastic-rigid setting, going to elastic-elastic should also be feasible.

To account for the aforementioned contact condition, some nodes, which do not overlap with nodes restricted either vertically or horizontally by Dirichlet boundary conditions, must be considered as potential contact nodes. The distance of a potential contact node  $(x, y)$  from the restricting boundary is described by a gap function  $g(x, y)$ , which can be constructed to represent any arbitrary shaped obstacle through the equation  $g(x, y) = 0$ . Displacement of a finite element node  $i$  from its initial position  $\mathbf{x}_i = (x_i, y_i)$  by the displacement vector  $\mathbf{u}_i = (u_{ix}, u_{iy})$  to its current position  $\mathbf{x}_i + \mathbf{u}_i$  will result to the nodal gap  $g_i(\mathbf{u}_i) = g(x_i + u_{ix}, y_i + u_{iy})$  as a function of the nodal displacement vector  $\mathbf{u}_i$ . The unit normal vector at the considered node, pointing to the interior of the obstacle, is simply obtained by the spatial gradient of the gap function as

$$\mathbf{n}_i(\mathbf{u}_i) = - \frac{\nabla g}{\|\nabla g\|} \Big|_{\mathbf{x}=\mathbf{x}_i+\mathbf{u}_i}. \quad (1)$$

The impenetrability condition between a node and the restricting boundary is expressed in a nodal sense as

$$g_i(\mathbf{u}_i) \geq 0. \quad (2)$$

This means that, in between nodes, element sides are in general not prevented from passing the restricting boundary. However, in the simple case of a straight restricting boundary and linear Lagrangian elements, element sides between two potential contact nodes are sufficiently hindered from penetrating the boundary. For curved obstacles the amount of side penetration decreases with mesh refinement.

For studying problems with friction, the direction of motion of each potential contact node with respect to the rigid obstacle is also needed. Based on a backward Euler approximation, the relative velocity vector  $\mathbf{v}_i$  at a node  $i$  can be written as

$$\mathbf{v}_i = \frac{\mathbf{u}_i - \mathbf{u}_i^{\langle t-\Delta t \rangle}}{\Delta t} - \mathbf{v}_0 \quad (3)$$

where  $\mathbf{v}_0$  describes the velocity of the rigid obstacle,  $\Delta t$  is the time step and  $\mathbf{u}_i^{\langle t-\Delta t \rangle}$  is the displacement of the considered node at the previous time instant  $t - \Delta t$ . Eq. (3) represents a single time step within a transient simulation, which is in generally necessary for capturing the load path dependence of contact tractions in the presence of Coulomb friction. However, in order to overcome the dependence of the final state on the whole deformation history of the considered structure, examples are chosen here such that the direction of frictional forces can reliably estimated in a single load increment. This is mainly achieved by adopting a loading with a single and monotonically increasing component but

also by prescribing a relative velocity between the contact bodies that ensures pure sliding. In general though, for problems without a dominant relative motion direction, accounting for the entire time history will be inevitable unless an approximation such as the likely-state approach by Hilding and Klarbring [26] is used.

For the simple examples studied in the present work, a single load step is nevertheless sufficient and the undeformed configuration is adopted as the previous time step configuration, i.e.  $\mathbf{u}_i^{(t-\Delta t)} = 0$ . For Coulomb friction, where the friction force is independent of the magnitude of the sliding velocity, the choice of  $\Delta t$  and the scaling of  $\mathbf{v}_0$  are inessential. For the examples involving pure sliding though, it must simply be ensured that the product  $\mathbf{v}_0 \Delta t$  is larger than any elastic deformation in order to exclude sticking at any node. Throughout this work  $\Delta t = 1\text{s}$  is used.

The impenetrability condition (2) alone is not sufficient for determining the two unknown components of the nodal contact force vector  $\mathbf{f}_i^c = \{f_x^c \ f_y^c\}^T$  on a potential contact node  $i$ . For a given friction law, a certain relation between its normal and tangential components needs to be fulfilled upon frictional sliding. For Coulomb friction, as demonstrated in [29, 30], the impenetrability, friction and relevant complementarity conditions can be expressed through a single non-smooth equality condition

$$\mathbf{C}(\mathbf{f}_i^c, g_i, \mathbf{v}_i, \mathbf{n}_i) = \mathbf{0} \quad (4)$$

for each potential contact node  $i$ . It should be noted here that both the gap function  $g_i$ , the unit normal  $\mathbf{n}_i$  and the velocity vector  $\mathbf{v}_i$  all are functions of the unknown displacement vector  $\mathbf{u}_i$ . The non-smooth vector-valued  $\mathbf{C}$ -function is defined as

$$\mathbf{C}(\mathbf{f}_i^c, g, \mathbf{v}, \mathbf{n}) = \mathbf{f}_i^c + [\mathbf{f}_i^c \cdot \mathbf{n} + rg]_- \mathbf{n} - P_{B(\mathbf{n}, \mu[\mathbf{f}_i^c \cdot \mathbf{n} + rg]_-)}(\mathbf{f}_i^c - r\mathbf{v}) \quad (5)$$

where  $\mu$  is the Coulomb friction coefficient and  $r$  is an augmentation parameter that may be chosen freely as long as  $r > 0$ . Though, for numerical reasons  $r$  needs to be selected according to the study performed in [31]. The value used for  $r$  is included for each of the test examples. The negative part operator  $[\cdot]_-$  is defined as

$$[x]_- = \begin{cases} -x & \text{if } x \leq 0 \\ 0 & \text{if } x > 0 \end{cases} \quad (6)$$

and  $P_{B(\mathbf{n}, \tau)}(\mathbf{d})$  is a projection of vector  $\mathbf{d}$  onto the plane with the normal vector  $\mathbf{n}$  and within a circle of radius  $\tau$ . The projection is defined as

$$P_{B(\mathbf{n}, \tau)}(\mathbf{d}) = \begin{cases} \mathbf{T}_n \mathbf{d} & \text{if } \|\mathbf{T}_n \mathbf{d}\| \leq \tau \\ \tau \frac{\mathbf{T}_n \mathbf{d}}{\|\mathbf{T}_n \mathbf{d}\|} & \text{otherwise} \end{cases} \quad (7)$$

where  $\|\cdot\|$  is the Euclidean norm and  $\mathbf{T}_n$  is the tangent plane projection defined as

$$\mathbf{T}_n = \mathbf{I} - \mathbf{n} \otimes \mathbf{n}. \quad (8)$$

When  $\mathbf{u}$  and  $\mathbf{f}^c$  are considered to be the global assembled vectors, containing all nodal displacements  $\mathbf{u}_i$  and contact forces  $\mathbf{f}_i^c$ , it is possible to write one final set of global residual equations

$$\begin{aligned}\mathbf{R}_u &= \mathbf{K}\mathbf{u} - \mathbf{f}^c - \mathbf{f}^{ext} = \mathbf{0} \\ \mathbf{R}_c^{<i>} &= -\frac{1}{r}\mathbf{C}(\mathbf{f}_i^c, g_i, \mathbf{v}_i, \mathbf{n}_i) = \mathbf{0} \quad i = 1, \dots, n_c\end{aligned}\tag{9}$$

governing the unknown structural displacements  $\mathbf{u}$  and contact forces  $\mathbf{f}^c$ . In this definition of  $\mathbf{R}_u$ ,  $\mathbf{K}$  is the global linearized elasticity stiffness matrix. Compared to their standard form, without contact, the residual equations governing nodal displacements  $\mathbf{R}_u$  are slightly modified here by accounting for the contact forces by the subtraction of  $\mathbf{f}^c$  apart from the external forces vector  $\mathbf{f}^{ext}$ . This term couples nodal displacements and contact forces. The contact condition residual  $\mathbf{R}_c^{<i>}$  contains the two components of the respective assembled residual vector  $\mathbf{R}_c$  corresponding to node  $i$ . The latter will hence depend nonlinearly on both  $\mathbf{u}$  and  $\mathbf{f}^c$ . Note, that  $n_c$  is the number of potential contact nodes. For its linearization with respect to each of the unknowns, the piecewise defined partial derivatives of the  $\mathbf{C}$ -function from [30] are necessary, cf. Appendix A. The factor of  $-1/r$  in the definition of  $\mathbf{R}_c^{<i>}$  is for ensuring a close to symmetric total system matrix, and hence it is included only for numerical reasons. After linearization, the residual equations of Eq. (9) are solved to obtain the state vector  $\mathbf{s} = \{\mathbf{u} \quad \mathbf{f}^c\}^T$ , using a standard, full step, Newton Raphson scheme. It should be noted that the system Jacobian is in general nonsymmetric, motivating the choice of an LU factorization based direct solver employed in this work.

### 3. Objective functions

Structural compliance is commonly used as an objective function to demonstrate new developments within the field of topology optimization [32, 33, 34, 35], and it has also been used in combination with contact conditions in [18, 20, 19, 21, 22]. Alternative and often equivalent measures of compliance exist. For instance the two versions presented in Eq. (10) are commonly seen

$$\varphi = \mathbf{u}^T \mathbf{f}^{ext} \tag{10a}$$

$$\phi = \mathbf{u}^T \mathbf{K}\mathbf{u} \tag{10b}$$

For static linear problems the two forms in Eq. (10) are equivalent, but especially for problems with unilateral contact, the possibility of rigid body motion, renders this equivalence invalid. For example, rigid body motion is likely to occur not only in the absence of sufficient supports but also when a design disconnects from the available supports and subsequently only uses

the contact surfaces as anchor points. For compliance optimization we use the compliance definition in Eq. (10b) as this form is not sensitive to rigid body motions.

However, compliance can often play a secondary role in real life applications where the distribution of interface tractions can be of particular interest instead. This is for example the case for spline shaft couplings, gear pairs, brake pads and joint replacement implants. To cover this need, a new objective function is proposed, aiming at minimizing both the magnitude and the variation of normal contact forces within an a priori unknown sub-region of a predefined interface. Assuming that unilateral contact can possibly occur within the given boundary  $\Gamma$ , we propose to minimize the following quantity

$$\bar{\psi} = \frac{\int_{\Gamma} p^q d\Gamma}{\int_{\Gamma} \mathcal{H}(p) d\Gamma} \quad (11)$$

in which  $p$  is the contact pressure and  $\mathcal{H}$  is the discontinuous Heaviside step function defined as

$$\mathcal{H}(x) = \begin{cases} 0 & \text{if } x < 0 \\ 1 & \text{if } x \geq 0 \end{cases}. \quad (12)$$

The exponent parameter  $q$  can be used to alter the behavior of the objective function. Increasing  $q$  contributes to the penalization of variations in the distribution of  $p$ , so that for larger values of  $q$  the obtained pressure distribution is expected to be closer to uniform compared to lower values of  $q$ .

Of course, Eq. (11) is limited to cases where a potential contact boundary  $\Gamma$  is known. The actual area of contact to be determined as part of the optimization has to lie within this predefined boundary  $\Gamma$ . For small deformation problems with rigid obstacles as the ones considered here, it is reasonable to assume contact at the boundary of the design domain. In general however, an extension of the objective function to cases of a completely unknown contact interface, potentially also in the interior of the design domain, would certainly be useful, but is deemed outside the scope of this work.

An important observation is that the integral expression in Eq. (11) is not well-defined in cases without contact. That is, the denominator of Eq. (11) corresponds to the actual area of contact and hence division with zero may occur during the optimization if no contact-zone is present. To alleviate this problem and avoid division by zero, it is convenient to limit the denominator by a minimum value  $\epsilon$ . Moreover, considering that  $\Gamma$  is discretized using a number of nodes indexed with  $i$ , a discrete and regularized form of Eq. (11) can be obtained as

$$\tilde{\psi} = \frac{\sum_i a_i p_i^q}{\max\{\epsilon, \sum_i a_i \mathcal{H}(p_i)\}} \quad (13)$$

where  $a_i$  and  $p_i$  respectively are the area and pressure associated with contact node  $i$ . In two dimensions, the constant nodal-associated area  $a_i$  is simply

obtained by summing the half areas of the elements adjacent to node  $i$ . The  
 275 normal pressure  $p_i$  is then obtained from the nodal contact force vector  $\mathbf{f}_i^c$  as  
 $p_i = \mathbf{n}_i^T \mathbf{f}_i^c / a_i$ . Note, that the discontinuous Heaviside step function  $\mathcal{H}$  used in  
 Eq. (11) has been replaced by a regularized smooth version  $H$  defined as

$$H_{\beta,\eta}(x) = \frac{\tanh(\beta\eta) + \tanh(\beta(x - \eta))}{\tanh(\beta\eta) + \tanh(\beta(1 - \eta))} \quad (14)$$

where  $\eta = 0$  and  $\beta = 1024$  are the threshold value and the steepness parameter  
 respectively. Since the argument of  $H$  in Eq. (13) is always non-negative, this  
 280 choice creates a very steep transition from  $H(0) = 0$  to  $H(0^+) \rightarrow 1$ . We are  
 aware that a  $\beta$ -value of 1024 seems extreme, but numerical experiments show  
 that it works as intended.

By choosing a small positive  $\epsilon$ , compared to  $a_i$ , Eq. (13) avoids division by  
 zero in cases where there is no contact, while the exact objective function is  
 285 recovered once at least one element is in contact. However, the presence of the  
 max operator results in a continuous but non-smooth objective function. In  
 order to work with a continuously differentiable objective function, we propose  
 another formulation, where the onset of contact is also accounted for through  
 the smooth Heaviside function  $H$ . This is done by replacing the denominator of  
 290 Eq. (13) as shown in the following expression

$$\psi = \frac{\sum_i a_i p_i^q}{\sum_i a_i H(p_i) + \left[1 - H\left(\sum_i a_i p_i\right)\right] \epsilon} \quad (15)$$

In this expression, the effect of  $\epsilon$  vanishes progressively as the total contact force  
 increases from zero to positive values. This ensures a smooth transition of the  
 objective function when going from a configuration of no contact to a configu-  
 ration with contact and vice versa. All further derivations in the present work  
 295 concern the objective function according to Eq. (15) with the value  $\epsilon = 0.01 a_i$   
 used for all numerical examples of pressure optimization.

The four cases presented in figure 1 illustrate the behavior of the proposed  
 objective function for different representative contact pressure distributions. For  
 $q > 1$ , a uniform distribution of contact forces results in the lowest objective as  
 300 desired.

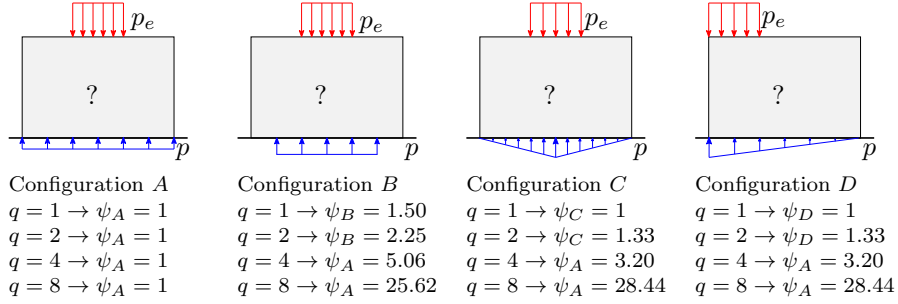
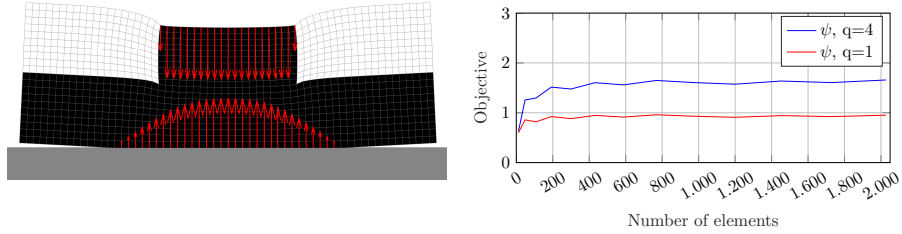


Figure 1: Four different contact pressure distributions resulting from an applied pressure  $p_e = 3$  Pa, corresponding to a total external force  $F_e = 1$  N. The objectives for  $q = \{1\ 2\ 4\ 8\}$  are included for all configurations. The width of the domain is 1 m and the height is  $2/3$  m.

To demonstrate that the proposed objective function is also mesh-independent a small numerical example is conducted. The structure shown in figure 2a is solved on multiple meshed with decreasing element size and the resulting objective values are plotted for  $q = 1$  (red) and  $q = 4$  (blue) in figure 2b. The mesh refinement is the same in both spatial directions such that elements remain square.



(a) A structure discretized into  $60 \times 20$  elements. Displacements magnification is  $10^5$ .

(b) Objective values for  $q = 1$  and  $q = 4$  as a function of the number of elements used in the discretization.

Figure 2: Impact of mesh refinement on the objective function. The width of the structure is 2 m and the height is  $2/3$  m. Black elements represent solid material with an elasticity modulus of  $E = 1$  MPa and white elements represent void with an elasticity modulus of  $E = 10^{-9}$  MPa. The Poisson's ratio for all elements is  $\nu = 0.3$ . The external load corresponds to a total force  $F_e = 1$  N.

For  $q = 1$  the objective represents the average contact pressure. As shown in figure 2a the contact forces span roughly half of the domain width, i.e. approximately 1 m. Hence, for a unit thickness and a total load of 1 N, the objective function should be  $\psi \approx 1$  Pa, which actually seems to be the case in figure 2b. The oscillations of the objective values seen in figure 2 occur as the nodal force at the left- and rightmost contact nodes may vary among very coarse meshes. However, the objective value converges towards a constant value as the mesh is refined.

#### 315 4. Topology optimization formulation

This section presents two topology optimization formulations, one for compliance minimization, as e.g. in [13] but in the robust framework proposed in [14], and a contact pressure optimization formulation based on the new objective function from Eq. (15), still in the same framework.

320 The general purpose robust topology optimization framework according to [14] is characterized by the three physical design fields  $\tilde{\rho}_e$ ,  $\tilde{\rho}_b$  and  $\tilde{\rho}_d$ , representing an intermediate blueprint design along with an eroded (over-etched) and a dilated version (under-etched). The physical design realizations are all obtained from the base mathematical design field  $\rho \in [0, 1]^{n_e}$  using a series of  
325 filter operations.

First, a convolution type density filter is applied to the design field following [36]. This filter computes the weighted average of the design variables within a predefined neighborhood,  $N_i$ , of radius  $r_{min}$ , which can be formally stated as

$$N_i = \{k \mid \|\mathbf{x}_k - \mathbf{x}_i\| < r_{min}\} \quad (16)$$

where  $\mathbf{x}_k$  denotes the geometrical center of element  $k$ . The filtered density of  
330 element  $\tilde{\rho}_i$  can now be obtained as

$$\tilde{\rho}_i = \frac{\sum_{k \in N_i} w(\mathbf{x}_k - \mathbf{x}_i) V_k \rho_k}{\sum_{k \in N_i} w(\mathbf{x}_k - \mathbf{x}_i) V_k} \quad (17)$$

where  $w(\mathbf{x})$  is the linearly decaying cone shaped function

$$w(\mathbf{x}) = r_{min} - \|\mathbf{x}\| \quad (18)$$

and  $V_k$  refers the volume of element  $k$ . We remark that the density filter by construction introduces intermediate densities and therefore that an additional filter is needed to ensure solid-void designs.

335 The output from the density filter is then passed through a smooth Heaviside function  $H_{\beta, \eta}$  as presented in Eq. (14). By employing different offsets for the threshold parameter  $\eta$ , it is possible to construct multiple realizations corresponding to either over- and under-etching of the blueprint design. Thus, in order to render the physical design insensitive to both over- and under-etching  
340 a minimum of three realization is needed, i.e.  $\tilde{\rho} \rightarrow \tilde{\rho}_k$  for  $k \in \{e, b, d\}$ . This can be formally stated as

$$\tilde{\rho}_k = H_{\beta, \eta_k}(\tilde{\rho}) \quad (19)$$

where the steepness parameter  $\beta$  is increased gradually during the optimization process using a continuation scheme.

345 The general purpose robust formulation can be greatly simplified for minimum compliance problems, or any other problem in which full utilization of the available material will be beneficial for the objective. For such problems it is only necessary to evaluate the objective, in the present case compliance,

on the eroded design and to apply the volume constraint on the dilated design. Thus, only one forward finite element analysis is needed per iteration and the optimization problem can be formally presented as

$$\begin{aligned}
& \min_{\boldsymbol{\rho} \in \mathbb{R}^{n_e}} : \phi_e \\
& s.t : \frac{\bar{\boldsymbol{\rho}}_d^T \mathbf{V}}{V_d^* V_{\text{tot}}} - 1 \leq 0 \\
& : 0 \leq \rho_i \leq 1, \quad i = 1, \dots, n_e
\end{aligned} \tag{20}$$

where  $\phi_e$  is the compliance measure defined in Eq. (10b) for the eroded version of the structure. The residual vector  $\mathbf{R}$  corresponds to both parts of Eq. (9) and it therefore involves both parts  $\mathbf{u}$  and  $\mathbf{f}^c$  of the state vector  $\mathbf{s}$ . Its explicit dependence on the physical density field  $\bar{\boldsymbol{\rho}}$  is through the elastic modulus  $E$  which is defined for each element  $i$  according to the modified SIMP relation

$$E_i = E_V + \bar{\rho}_i^{p_{SIMP}} (E_S - E_V) \tag{21}$$

where  $E_S$  and  $E_V$  are elastic moduli of solid and void respectively, and a stiffness penalization exponent  $p_{SIMP} = 3$  has been adopted. The contribution of element  $i$  to the global elasticity stiffness matrix  $\mathbf{K}$  is found as  $\mathbf{K}_i = E_i \mathbf{K}_0$ , where  $\mathbf{K}_0$  is the element stiffness matrix for a unit elastic modulus. For this optimization problem, the use of the penalized stiffness interpolation scheme SIMP [1, 37] will by construction favor black and white designs. However, without the projection filter and the robust formulation, an intrinsic region of intermediate densities of size  $r_{min}$  will persist due to the density filtering. Although other methods exist to suppress the intermediate densities, e.g. [15] or [16], we choose to apply a smooth Heaviside filter in combination with the robust design formulation. This means that the volume constraint is enforced on the dilated design, which is sufficient due to the nature of the minimum compliance, i.e. the objectives will always follow  $\phi_e > \phi_b > \phi_d$  and the opposite for the volumes. The material constraint is updated every 20 iteration by redefining  $V_d^* = V^* V_d / V_b$  such that the amount of material in the intermediate design  $V_b$  satisfies the prescribed volume fraction  $V^*$ . The individual volumes of all elements are stored in the vector  $\mathbf{V}$  and the total volume is denoted  $V_{\text{tot}}$ . Imposing the volume constraint in this way prevents the optimizer from exploiting the projection scheme as it is seen in [38], i.e. that intermediate densities remain in some of the optimized design realizations.

When optimizing for contact pressure according to the objective function from Eq. (15), there is no longer a predetermined relation between eroded, blueprint and dilated designs and the numerical value of the associated objective functions. Therefore, all considered design realizations must be evaluated by finite element analysis. To render the optimized designs insensitive to both over- and under-etching, we choose to use all three realization in the following, but remark, that two realizations are enough to ensure a length scale as well as

crisp solid-void designs. The resulting optimization problem can therefore be cast as follows

$$\begin{aligned}
\min_{\boldsymbol{\rho} \in \mathbb{R}^{n_e}} : & \max_k (\psi_k), \quad k \in \{e, b, d\} \\
s.t : & \frac{\bar{\boldsymbol{\rho}}_d^T \mathbf{V}}{V_d^* V_{\text{tot}}} - 1 \leq 0 \\
& : \frac{\varphi^* \varphi_e}{\varphi_0} - 1 \leq 0 \\
& : 0 \leq \rho_i \leq 1, \quad i = 1, \dots, n_e
\end{aligned} \tag{22}$$

385 Here the goal of the robust formulation is to minimize the largest of three objective values, obtained from three structural realizations  $\bar{\boldsymbol{\rho}}_k$ . Although this requires the solution of three finite element problems, we emphasize that these are completely decoupled and can be solved in parallel. In short, the increase in computational cost does not necessarily lead to an increase in run time.

390 The additional compliance constraint in Eq. (22) is necessary in order to prevent the optimizer from disconnecting the contact surface from the external load in order to reduce the contact pressure directly to zero at the cost of structural integrity. It is enforced on the eroded design and is expressed as a fraction  $\varphi^* \geq 0$  of the compliance  $\varphi_0$  corresponding to the initial design. For  
395 the compliance constraint, we will use the measure given in Eq. (10a). This choice of compliance measure is justified by the fact that the structures for which we perform pressure optimization cannot undergo rigid body motion. By increasing  $\varphi^*$  a stricter compliance condition is imposed on the final design.

400 The sensitivities of the two objective functions and the compliance constraint with respect to all relevant physical design fields  $\bar{\boldsymbol{\rho}}_k$  can be found efficiently by the adjoint method (with two right-hand sides) and subsequent application of the chain rule to take the filtering and projections into account. The adjoint problems are as follows:

$$\begin{aligned}
\mathbf{J}^T \boldsymbol{\lambda}_1 &= -\partial_{\mathbf{s}} \psi_k & \text{and} & & \partial_{\bar{\boldsymbol{\rho}}_{k,i}} \psi_k &= \mathbf{d}_{\bar{\boldsymbol{\rho}}} \psi_k + \boldsymbol{\lambda}_1^T \begin{pmatrix} \partial_{\bar{\boldsymbol{\rho}}_k} \mathbf{K} \mathbf{u} \\ \mathbf{0} \end{pmatrix} \\
\mathbf{J}^T \boldsymbol{\lambda}_2 &= -\partial_{\mathbf{s}} \varphi_e & \text{and} & & \partial_{\bar{\boldsymbol{\rho}}_{e,i}} \varphi_e &= \boldsymbol{\lambda}_2^T \begin{pmatrix} \partial_{\bar{\boldsymbol{\rho}}_e} \mathbf{K} \mathbf{u} \\ \mathbf{0} \end{pmatrix}
\end{aligned} \tag{23}$$

405 Here  $\boldsymbol{\lambda}_1$  and  $\boldsymbol{\lambda}_2$  are two sets of Lagrange multipliers and  $\mathbf{J}$  is the non-symmetric Jacobian of the system of Eqs. (9), evaluated at the final state, already available from the solution of the forward problem. Both adjoint problems are linear and presented in more detail in appendix B.

410 During the optimization, a  $\beta$ -continuation approach is used to gradually force the physical fields into a solid/void state. For all problems included in this work (unless otherwise stated)  $\eta \in \{0.7, 0.5, 0.3\}$ , the continuation starts with  $\beta = 1$  and  $\beta$  is doubled either after 50 design updates or whenever  $\|\Delta \boldsymbol{\rho}\| < 0.01$ . The continuation is terminated when the non-discreteness measure  $M_{nd}$  of the

blueprint design becomes less than 3%.  $M_{nd}$  is defined according to [39] as

$$M_{nd} = \frac{4\bar{\rho}_b^T(1 - \bar{\rho}_b)}{n_e} \cdot 100\% \quad (24)$$

where  $n_e$  is the number of design variables.

415 The contact solver, filters, sensitivity analysis and optimization problem are implemented in Matlab, and the design updates are performed using the Method of Moving Asymptotes by Svanberg [40].

## 5. Results

Figure 3 introduces the three test problems used for the numerical examples.

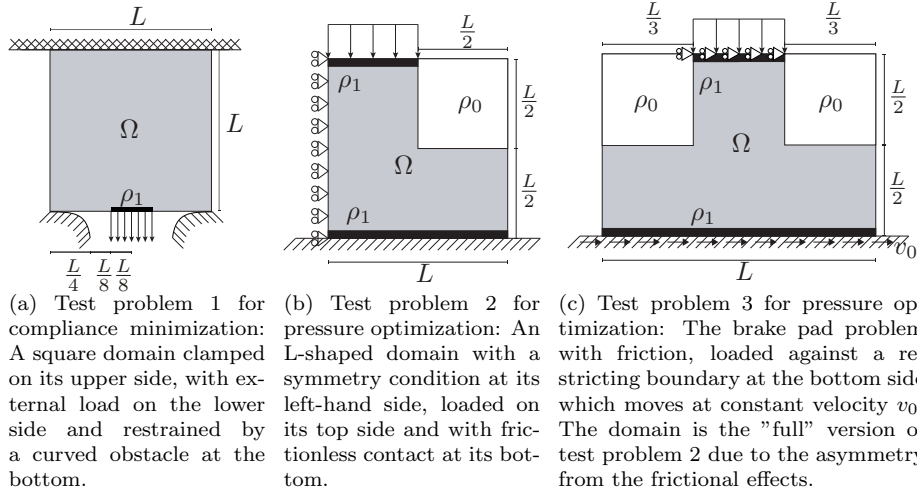


Figure 3: Schematic representations of the test problems used in the following sections. In the design domain  $\Omega$ ,  $\rho_0$  and  $\rho_1$  respectively denote elements prescribed as void and solid.

420 Test problem 1 presented in figure 3a is the benchmark compliance optimization problem presented e.g. in [19]. The problem consists of a square domain fully clamped on the upper boundary and subject to a downward distributed load around the center of the lower boundary. The obstacle is placed such that there is no initial gap between the lower corners of the domain and the obstacle.

425 A single row of elements is prescribed to be solid just above the anchoring of the external load. The obstacle is described by a function that transitions smoothly from a low slope within the outer two quarters of the domain to a steep bell function in the central half of the domain.

430 Applications of the proposed pressure based objective function are demonstrated through the test problems of figures 3b and 3c. Test problem 2 involves an L-shaped design domain, resting on a frictionless restricting boundary at the bottom and subject to a compression on one half of the upper side. This

example is constructed to demonstrate the design optimization for an even distribution of contact pressure in a simple configuration without frictional effects.

435 As illustrated in figure 3b, all nodes on the left side of the domain are horizontally constrained, corresponding to a symmetry condition about this axis. Moreover, the upper and lower sides of the domain are prescribed to be solid. Because of the unilateral contact condition, portions of the domain are free to move upwards, separating from the obstacle. In that sense, the actual contact  
440 area depends on the specific material distribution and the applied force.

Test problem 3 is an extension of problem 2 with frictional effects. In this case, a horizontal velocity is prescribed to ensure slip between the elastic domain and the obstacle. Due to the inclusion of friction and slip, symmetry cannot be exploited anymore, hence the entire design domain is considered with  
445 its upside-down T shape. The objective of this problem is to demonstrate how the optimized material distribution is affected by including a varying amount of friction. As in the previous case, the upper and lower boundaries are prescribed to be solid. Moreover, in order to accommodate the frictional forces, all nodes subject to external vertical load are at the same time constrained in the  
450 horizontal direction.

From a mathematical point of view, external forces could also act on not fully solid material. In all three test problems however, elements directly loaded through external forces are prescribed to be solid. This is simply to achieve more physical designs without much grey material in the vicinity of the applied  
455 load. The reason for adding a row of solid material at the contact interface for test problem 2 and 3 simply follows the same argument, and having such a predefined interface could be a typical design specification. We demonstrate that the material at the contact interfaces does in fact not need to be predefined in test problem 1 where the optimizer determines the interface by itself.  
460 Though still, the contact must occur at the boundary of the domain. One could potentially include all internal nodes of the design domain as potential contact nodes, but this would increase the degrees of freedom of the system and also raise the question of how to strictly define the area associated with each contact node, especially on a potential staircase interface. For this reason, we restrict  
465 ourselves to a known possible interface region, but without fixing beforehand the actual area of contact within this interface region.

Numerical parameters for each problem are included in table 1. For all three problems, the design domain is discretized by bilinear square elements.

	Description	Unit	Problem 1	Problem 2	Problem 3
$L$	Length scale	m	0.2	200	150
$R$	Density filter radius	m	$\frac{2}{100}L$	$\frac{3}{200}L$	$\frac{4}{100}L$
$E_S$	Elasticity of solid	N/m <sup>2</sup>	$2.1 \cdot 10^{11}, 2.1 \cdot 10^7$	$10^6$	$10^6$
$v_0$	Prescribed velocity	m/s	0	0	1
$r$	Augmentation parameter	m	$10^3$	1	1
	Number of elements		$192 \times 192^\dagger$	$200 \times 200$	$180 \times 120$

Table 1: Parameters used in the test problems. For all problems Poisson’s ratio is  $\nu = 0.3$ , the penalization parameter is  $p_{SIMP} = 3$ , Young’s modulus of void is  $E_V = 10^{-9}E_S$ .  
 $\dagger$ : only  $96 \times 192$  (half domain) was actually computed. Symmetry about  $x = 0.1m$  was utilized to present the results.

Generally speaking, from an undeformed state, the Newton Raphson algorithm needs less than 10 iterations to converge to an Euclidean norm of the residual vector smaller than  $10^{-9}$  times the Euclidean norm of  $\mathbf{f}^{ext}$ . The three control parameters of the MMA are set to `asyinit` = 1.07, `asydecr` = 0.65 and `asyinit` = 0.2. Before feeding the MMA with the objective values and the gradients, the objective is scaled to be 1 on the first iteration. For all of the following numerical examples the initial design is defined by a uniform density distribution sharply fulfilling the volume constraint.

### 5.1. Compliance optimization with contact

In this section we revisit the compliance minimization benchmark problem that has been studied in [18, 19, 20, 21]. The problem is also included in the review paper [41] and a schematic representation of the problem is depicted in figure 3a for reference. In [20] the initial gap between the structure and the obstacle, in case of no obstacle offset, is given by

$$g(x) = k_2 x^4 \quad \text{for } 0 \leq x \leq 0.05m \quad (25)$$

where  $x$  is the distance from the corner of the square domain. The value  $k_2 = 0.64m^{-3}$  is given in the reference but there is no definition of the gap for  $0.05m < x < 0.5m$ . To remove any ambiguity in the definition of the obstacle we use the gap function that is presented in Eq. (26). This function is a smooth step function defined for every point  $(x, y)$ , and the restricting boundary of the obstacle is defined as the curve that satisfies  $g(x, y) = 0$

$$\begin{aligned} g(x, y) = & y + \frac{h_d}{4} (\tanh(s(d + x - x_c)) + 1) (\tanh(s(d - x + x_c)) + 1) \\ & + \frac{h_k}{8} (4 - (\tanh(s(d + x - x_c)) + 1)) (\tanh(s(d - x + x_c)) + 1) \\ & \times \left( (x - 2x_c)^4 (\tanh(s(x - x_c)) + 1) - x^4 (\tanh(s(x - x_c)) - 1) \right) \end{aligned} \quad (26)$$

The parameters  $x_c$ ,  $d$ ,  $h_d$ ,  $s$ , and  $h_k$  control the shape of the obstacle. The center of the hole is given by  $x_c = 0.1m$ , while  $d = 0.05m$  defines the hole radius

and  $h_d = 0.5m$  the hole depth. The parameter  $s = 500$  defines the sharpness of the transition to the flanks of the hole. Finally, the parameter  $h_k$  has the same meaning as  $k_2$  in Eq. (25), defining the curvature of the fourth order polynomial in the outskirts region. Figure 4 visualises the difference between the piecewise gap function in Eq. (25) and the smooth gap function of Eq. (26).

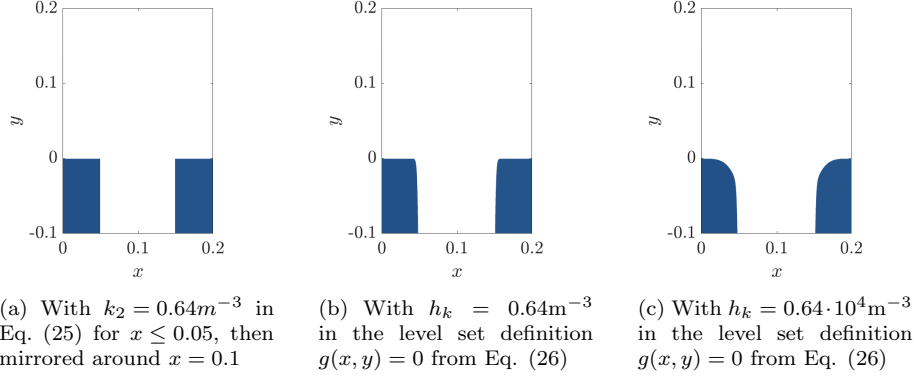


Figure 4: Obstacle representations. The outskirts appear to be flat for  $k_2 = h_k = 0.64m^{-3}$  even though they are described by a fourth order polynomial for  $0 \leq x \leq 0.05m$ .

For the rest of this section, we use the smooth representation of the obstacle based on Eq. (26). We first consider the obstacle geometry from Figure 4b, for  $h_k = 0.64m^{-3}$ , which best matches the available literature for this benchmark problem. Figure 5 summarizes the results of the problem for various load intensities and volume constraints, using the threshold values  $\eta \in \{0.7, 0.5, 0.3\}$ .

The design that is obtained for an external load of  $f^{ext} = 0.5kN$  and a volume fraction of  $V^* = 0.5$  resembles one of the designs presented in [20]. By increasing the load we are able to get results that resemble other designs presented in [20] where the obstacle is used as support. However, with a total load of  $0.1kN$  and an elasticity modulus of  $2.1 \cdot 10^5 MPa$  column designs will always emerge in contrast to the more interesting designs obtained for increased load. Generally, the designs that are obtained fall into three different categories listed below

1. Column designs. This type of design develops when it is not possible to take advantage of contact. This can happen if the external load is too small or the structure is too stiff.
2. Structures that are supported both on the upper and lower side of the domain. This type of design develops when contact can be exploited and enough material is available.
3. Disconnected structures. The optimizer may disconnect the design from the upper support and only use the obstacle as support when the available material is very scarce.

From the designs presented in figure 5 it can also be seen how it is possible  
520 to get combinations of the three types of structures listed above. For example,  
consider the design that is obtained for an external load of  $\mathbf{f}^{ext} = 12.5\text{kN}$  and  
a volume constraint of  $V^* = 0.5$ . This design is supported on both the upper  
and the lower side of the domain and it resembles a combination of a column  
design and a disconnected design.

525 A few more points can be made about the designs in figure 5 in relation to  
the location of the support that is created on the obstacle.

- Increasing the load causes the location of the support to contract towards  
the center of the domain. This yields a more compact structure. This is  
the case for all three types of designs listed above. This effect is rather  
530 small and may be hard to see by eye in the way the designs are presented  
here. The effect is best seen across the rows of figure 5.
- For structures that are supported on both the upper and lower side of the  
domain, the location of the emerging support will move outwards as more  
material is available due to the curvature of the obstacle. This effect is  
535 more pronounced and may be studied in the columns of figure 5.

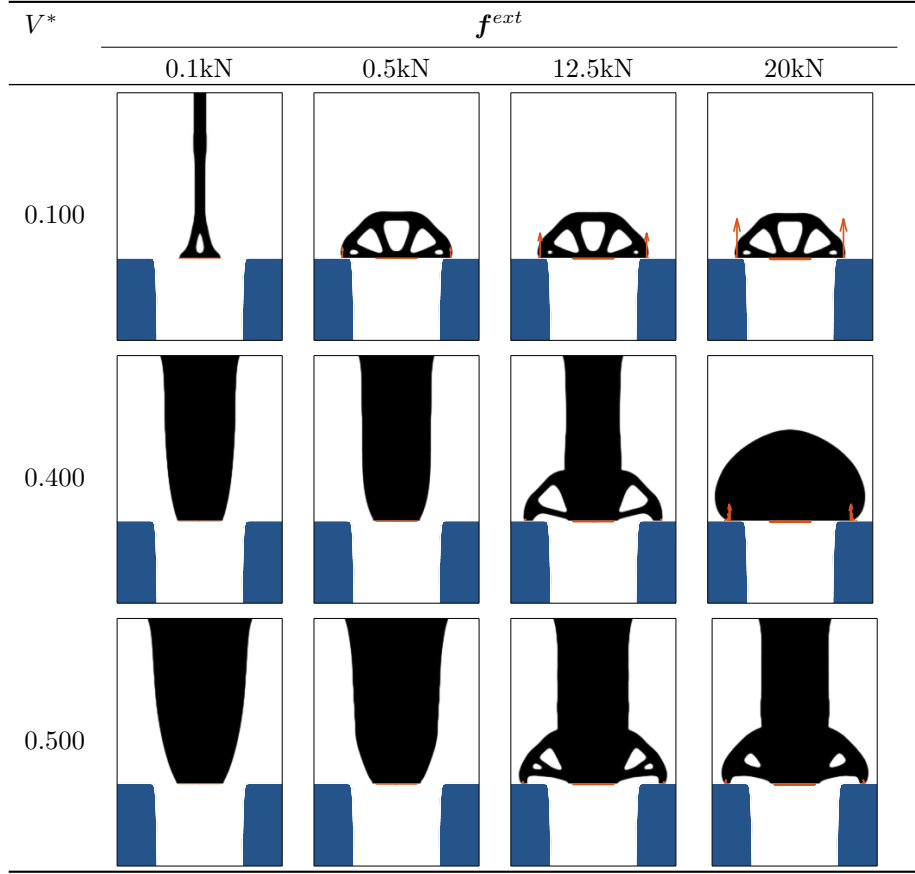


Figure 5: Solutions ( $\bar{\rho}_b$ ) to test problem 1, as schematized in figure 3a, where  $g(x, y)$  is defined as in Eq. (26) and  $h_k = 0.64\text{m}^{-3}$  for three different material constraints and three different magnitudes of external load. Please note, that reaction forces at the upper support are not illustrated here.

In order to add some complexity to this example, we now increase the constant  $h_k$  to  $0.64 \cdot 10^4\text{m}^{-3}$ , so that contact can take place on the large curved surface illustrated in figure 4c. In addition, we make the structure more compliant by reducing the elasticity modulus from  $E_S = 2.1 \cdot 10^{11}\text{Pa}$  to  $E_S = 2.1 \cdot 10^7\text{Pa}$  and we introduce Coulomb friction. The total external force applied is also slightly decreased, and in this case fixed, to 0.2kN. The compliance minimization problem is solved for a volume constraint of  $V^* = 0.1$  with and without a friction coefficient of  $\mu = 0.3$ . The results are presented in figure 6.

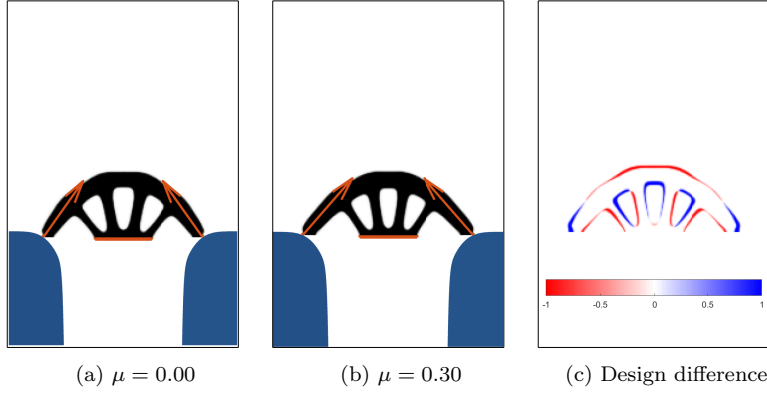


Figure 6: Solutions ( $\bar{\rho}_b$ ) to test problem 1, as schematized in figure 3a, where  $g(x, y)$  is defined as in Eq. (26) and  $h_k = 0.64 \cdot 10^4 \text{m}^{-3}$  without and with Coulomb friction. Total external load is  $\mathbf{f}^{ext} = 0.2 \text{kN}$  and elasticity modulus is  $E_S = 2.1 \cdot 10^7 \text{Pa}$ . (c) highlights how the design is changed by the inclusion of friction, by showing the difference between (a) and (b).

Figure 6 illustrates that the proposed method can be applied to more complex problems. Here, the optimizer takes advantage of the slope of the obstacle to build a compact design, that does not need a horizontal stiffener, as was the case for the disconnected designs in figure 5. Including friction allows the optimizer to build a wider structure as highlighted by figure 6c. Because of the friction, the optimizer needs not to rely as much on the curvature of the obstacle, but can instead utilize the friction to gain support.

To verify the optimization outcome, a cross-check on the performance of the optimized designs in figure 6 is performed by evaluating the compliance of each design in the opposite setting. Table 2 demonstrates that optimizing for a specific  $\mu$  yields the best-performing design for that particular  $\mu$ .

Analyzed for	Optimized for	
	$\mu = 0.0$	$\mu = 0.3$
$\mu = 0.0$	<b>0.0129</b>	0.0253
$\mu = 0.3$	0.0294	<b>0.0135</b>

Table 2: Compliance  $\phi_b$  for the designs presented in figure 6 evaluated with different friction coefficients (cross-checking to verify the optimization process).

A final observation from our numerical experiments concerns the role of the robust formulation in Eq. (20). That is, if only a single realization is considered, still including the density filter and the Heaviside projection, the resulting optimized designs exhibit significant contact forces in nearly void regions. This is despite the optimized designs reaching an MND of less than 1.5% and further motivates the use of the robust approach for contact problems, even when using compliance as objective.

### 5.2. Contact pressure optimization without friction

This section concerns test problems 2 and 3 from figure 3, where optimization of pressure distribution along the contact interface is performed according to Eq. (22) with the objective function from Eq. (15). The obstacle is defined by the simple level set function in Eq. (27), such that it coincides with the  $x$ -axis.

$$g(x, y) = y \quad (27)$$

Consider first test problem 2 with the objective function exponent  $q = 2$ , and the volume constraint  $V^* = 0.5$ . Results corresponding to solutions without a compliance constraint, i.e.  $\varphi^* = 0$ , as well as with a compliance constraint at  $\varphi^* = 1$ , are presented in figure 7.

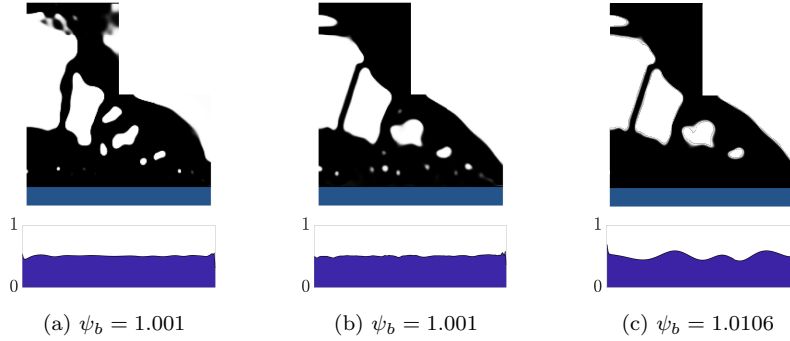


Figure 7: Comparison of three different designs obtained with  $V^* = 0.5$  and  $q = 2$ . (a): No compliance constraint,  $\psi^* = 0$ . (b): With compliance constraint  $\psi^* = 1$ . (c): Post-processed version of the structure in (b), with holes along the lower part of the domain filled with material, thus violating the volume constraint. The curve below each structure indicates the contact pressure along the lower edge of the domain.

In both figures 7a and 7b an even pressure distribution is achieved along the contact interface by directing some of the applied load to the lower right corner of the domain. When the compliance constraint is omitted, the structure of figure 7a is obtained with some porosity near the lower side of the domain and a non straight strut at the left side. By including the compliance constraint  $\varphi^* = 1$ , we obtain the design of figure 7b which resembles the design of figure 7a, but the strut has straightened out to increase the overall stiffness of the structure while the porosity near the contact interface has increased, i.e small holes have been introduced. We remark that solving the problem without a compliance constraint is highly ill-posed and that the thresholds was set to  $\eta \in \{0.51, 0.5, 0.49\}$  for both examples in order to allow for comparison. To investigate the importance of the small holes in figure 7b, a postprocessed version is presented in figure 7c. For this structure, the smaller holes at the bottom were filled with solid material and the analysis reveals how the suppressed porosity is essential for obtaining the even pressure distribution in figure 7b.

To further investigate the sensitivity of the design to manufacturing errors, strongly dilated and eroded version of the structure in figure 7b were evaluated.

Figure 8 shows three under- and one over-etched versions of the design from figure 7b and a plot of the objective value as function of  $\eta$ . In this case, the base design, obtained for  $\eta \in \{0.51, 0.50, 0.49\}$ , is more sensitive to over-etching than it is to under-etching.

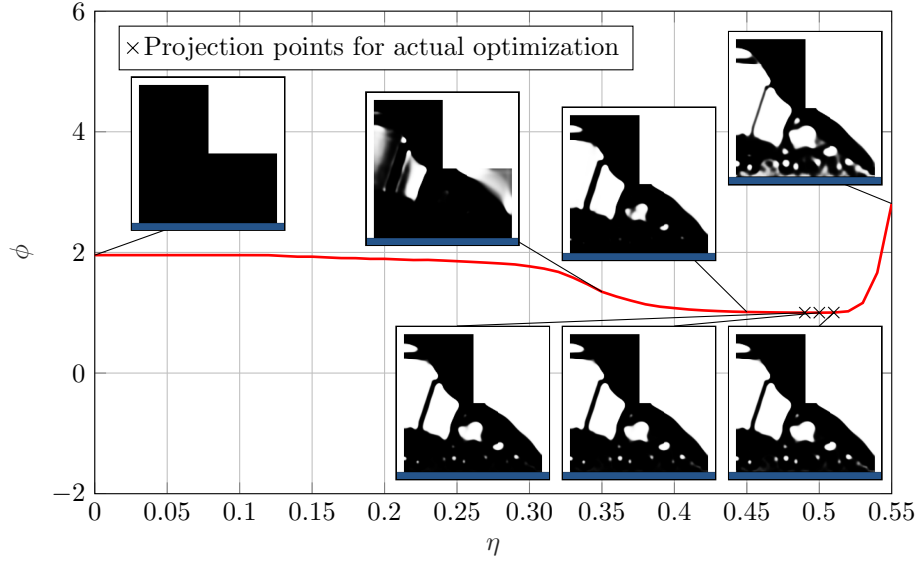


Figure 8: Analysis of how sensitive the design of figure 7b is to over- or under-etching.

After having demonstrated the role of including a compliance constraint and investigated the sensitivity of the designs to under- and over-etching, the remaining part of this subsection focuses exclusively on cases with constrained compliance and threshold values  $\eta \in \{0.7, 0.5, 0.3\}$ . Figures 9 through 11 show optimized designs from a parametric study with respect to the objective function exponent  $q$ , the volume constraint limit  $V^*$  and compliance constraint limit  $\varphi^*$ . Keeping in mind that the objective function is non-convex, there is no guarantee for the optimization to reach the global minimum; convergence to some local minimum is much more likely. However, a general tendency for all of the following results is that for a given volume constraint limit  $V^*$  the objective increases for more strict compliance constraints. Lower values of  $\varphi^*$  result in somewhat more uniform pressure distributions, while requiring a higher stiffness by increasing  $\varphi^*$  leads to fewer and stiffer beams and corresponding sites of pressure concentrations.

Three quantities are included for each design in all of the following figures: (1) the objective value  $\psi_b$ , (2) the mean and (3) the variance of all non-zero normal contact forces. The curves below each structure in figures 9 through 11 show the pressure distribution on the contact interfaces.

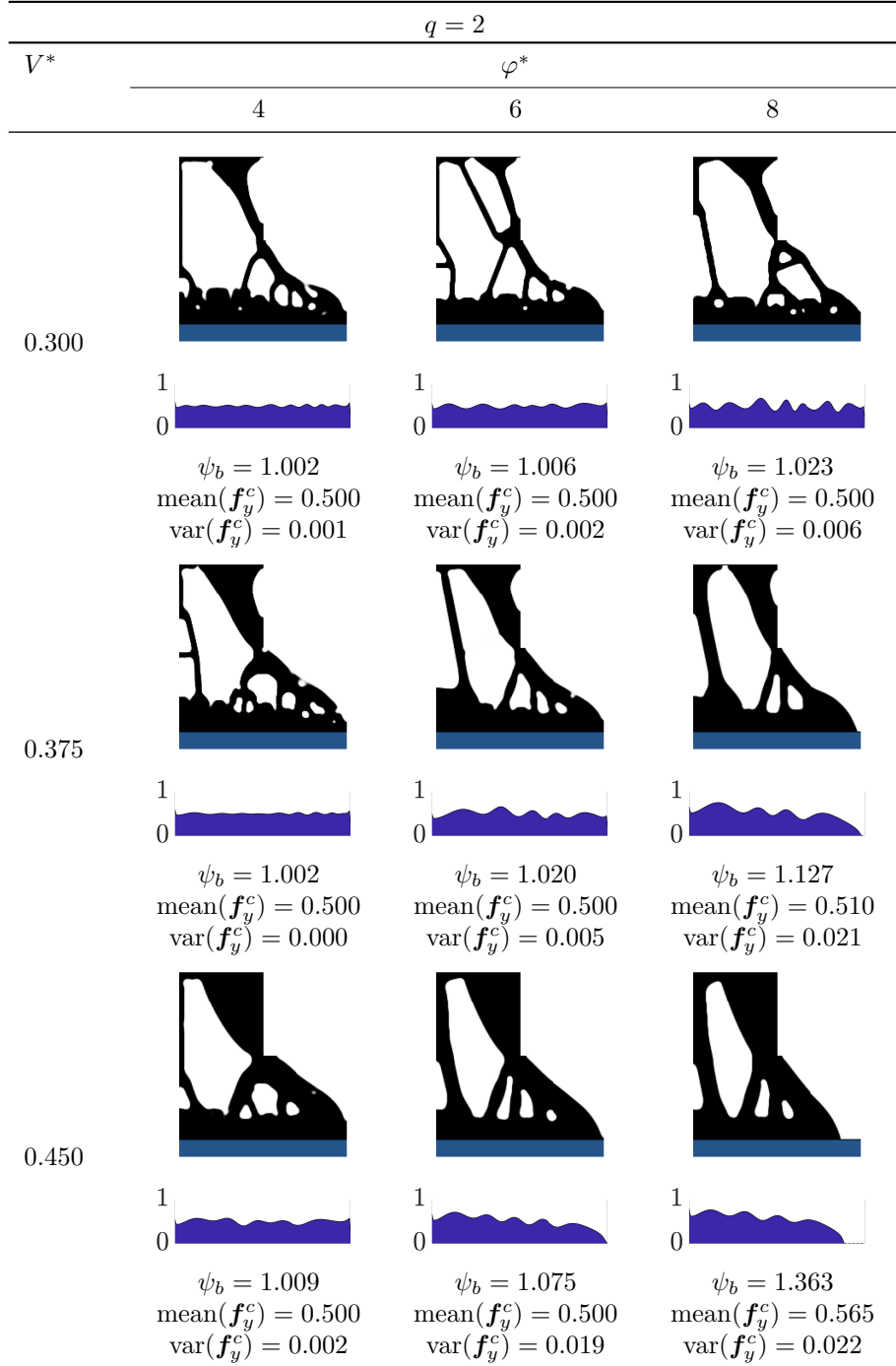


Figure 9: Solutions to test problem 2 as sketched in figure 3b solved for  $q = 2$  and various choices of  $V^*$  and  $\varphi^*$ . The curve below each structure indicates the contact pressure along the lower edge of the domain.

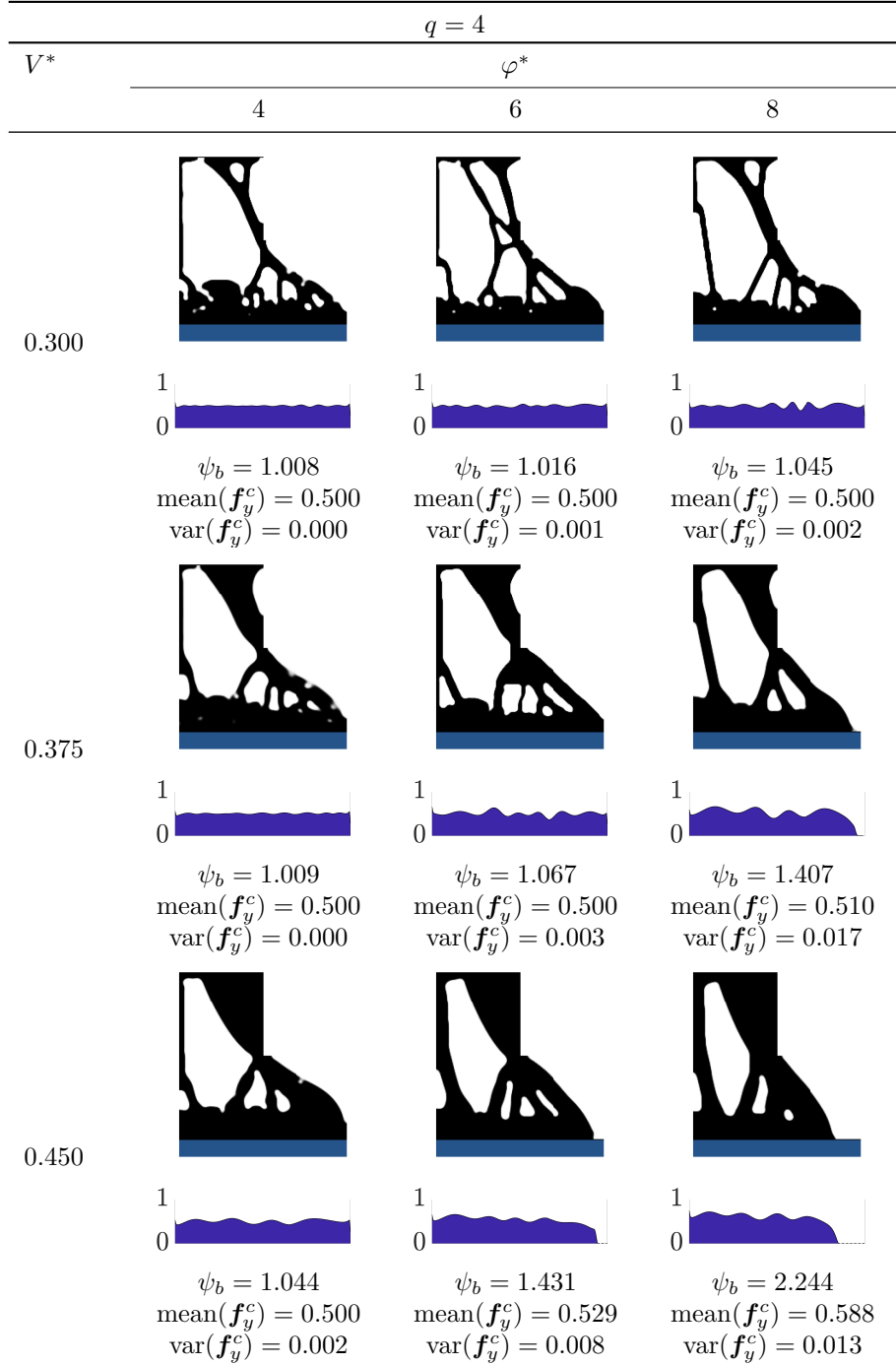


Figure 10: Solutions to test problem 2 as sketched in figure 3b solved for  $q = 4$  and various choices of  $V^*$  and  $\varphi^*$ . The curve below each structure indicates the contact pressure along the lower edge of the domain.

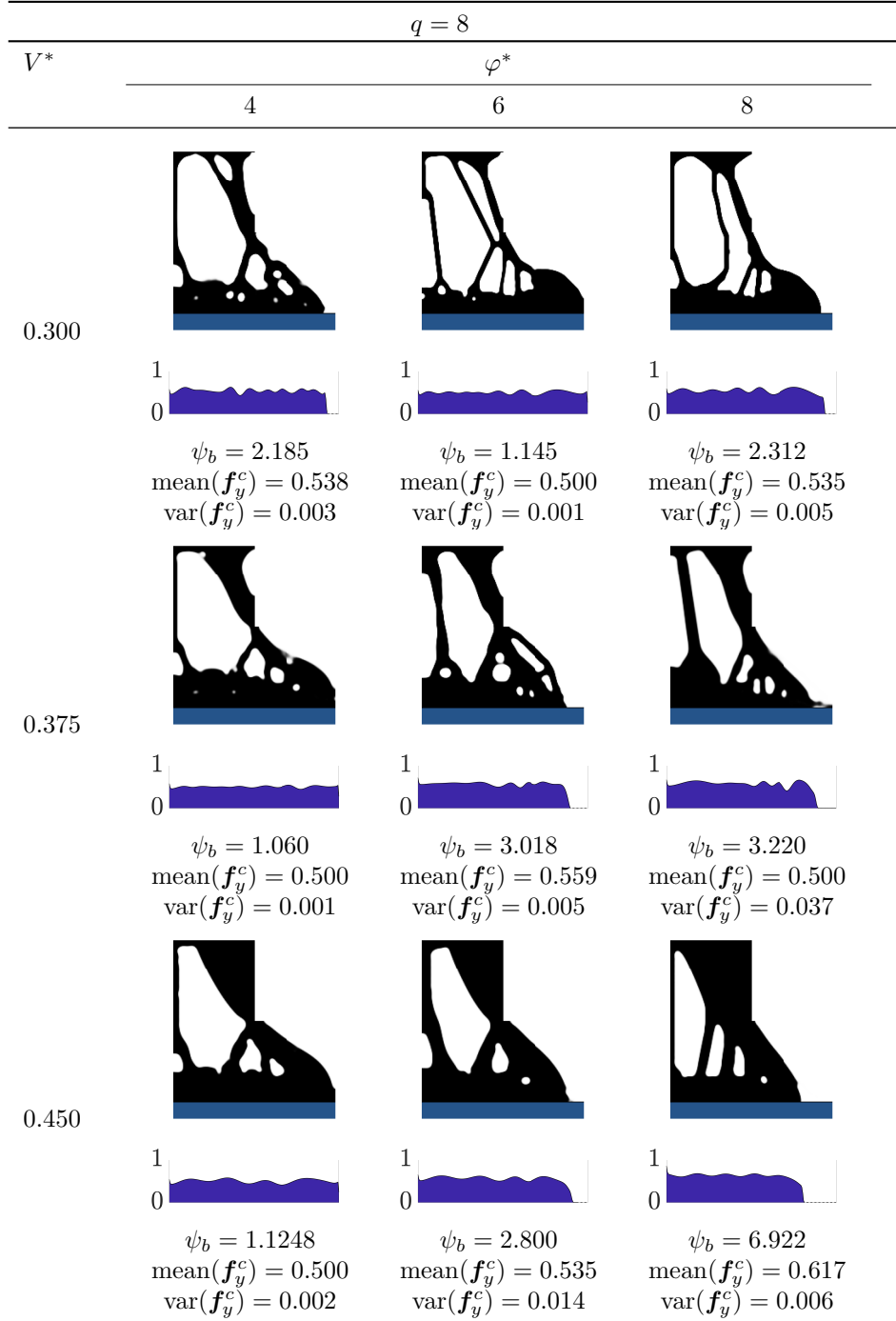


Figure 11: Solutions to test problem 2 as sketched in figure 3b solved for  $q = 8$  and various choices of  $V^*$  and  $\varphi^*$ . The curve below each structure indicates the contact pressure along the lower edge of the domain.

The objective values reported in figures 9 through 11 generally confirm that increasing  $\varphi^*$  causes the objective value to increase. This is expected, as there is less design freedom for the optimizer. The same conclusion applies if the variation of the contact forces is considered instead of objective values. Physically, increased variation of contact forces upon stiffening of the design is due to pressure concentrations below emerging pillars.

Figure 12 emphasizes the effect of increasing the objective function exponent  $q$  in the cases of  $V^* = 0.375$  and  $\varphi^* = 8$  extracted from figures 9 through 11. As  $q$  is increased, variations in the pressure distribution are penalized stronger. The pressure distribution appears most even in the case of  $q = 8$ . However, the actual contact area reduces as  $q$  is increased from 2 to 8, which indicates that the price paid for flattening out the pressure distribution while maintaining structural stiffness, is an increased average pressure.

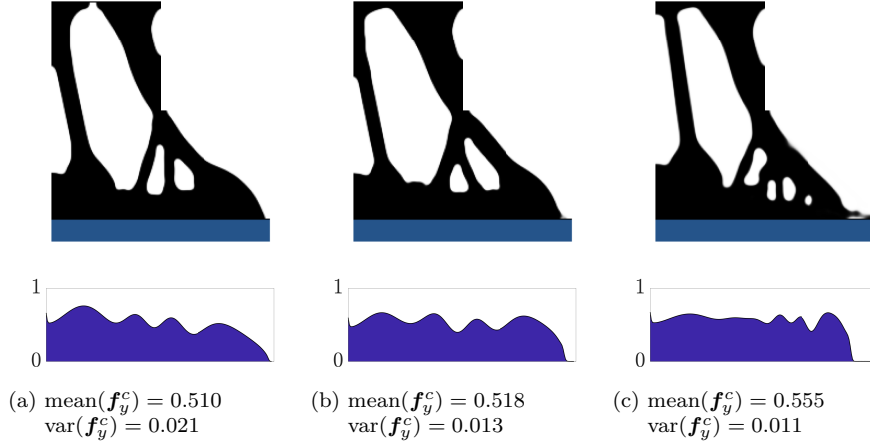


Figure 12: Test problem 2 solved with the following parameters:  $V^* = 0.375$  and  $\varphi^* = 8$  (a)  $q = 2$ , (b)  $q = 4$  and (c)  $q = 8$ . The curves below each structure indicates the contact pressure along the lower edge of the domain.

Figure 13 shows a convergence curve that is representative of all optimization problems of figure 9 through 11. It specifically corresponds to  $q = 4$ ,  $V^* = 0.3$  and  $\varphi^* = 4$  and it includes the evolution of the objective values and the constraints as functions of the iterations. Large peaks within the first 300 iterations are associated with the employed  $\beta$ -continuation. To amplify changes in the objective, the red curves of figure 13 show adjusted objective values,  $\psi'$  defined as

$$\psi'_k = \psi_k - \min(\psi_k) \quad (28)$$

in order to shift all objective values towards zero where small differences are most clear in logarithmic scale.

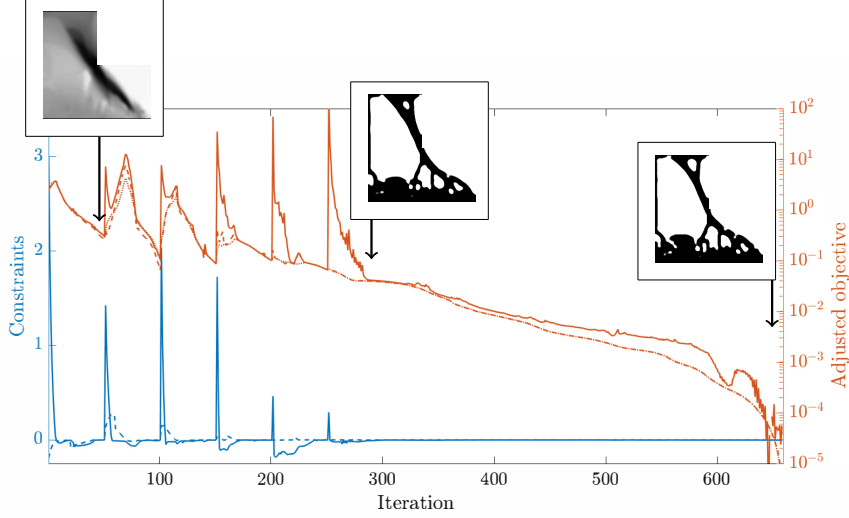


Figure 13: Convergence history for the design shown in figure 10 for  $V^* = 0.3$  and  $\varphi^* = 4$ . This is a typical convergence behavior for all structures in figure 9 through 11. The presented designs are shown after 50, 286 and 658 design updates respectively.

—: Compliance constraint    - - -: volume constraint    —:  $\psi'_e$     - - -:  $\psi'_b$     ···:  $\psi'_d$

We remark once again, that for this optimization problem it is necessary to perform the finite element analyses for all three cases of  $k \in \{e, b, d\}$ , as there is no way to determine which of the three realizations will have the largest objective for a particular iteration.

Generally, the  $\beta$  continuation is the main reason for the high number of required iterations, especially in cases where  $\beta$  cannot be doubled, but instead is incremented in steps of 1. It is likely that a fixed- $\beta$  approach [42], although out of the scope of this work, could alleviate this performance penalty. In terms of wall-clock time, the design shown in figure 13 takes roughly 1.5 hours to compute. Each iteration takes roughly 10 seconds (including everything and no parallelisation). Solving the state equations is the largest computational task of each iteration, thus one could employ various strategies to reduce this computational task. Obvious strategies to decrease the wall-clock time of these examples could be parallelisation or to use a reduced-order method for the linear elasticity equations.

### 5.3. Contact pressure optimization with friction

In this section, we study solutions to test problem 3. The problem is solved for three values of the Coulomb friction coefficient  $\mu$  to investigate the influence of friction on the design. The optimized design field is expected to depend on the direction of the prescribed surface velocity of the rigid body and the coefficient of friction. As Coulomb friction forces do not depend on the magnitude of the prescribed velocity, as long as slip occurs, the design is also unaffected

655 by the magnitude of the prescribed velocity. The following figures illustrate  
 six solutions to test problem 3 for three choices of  $\mu$  and two choices of the  
 objective function exponent  $q$ , using the threshold values  $\eta \in \{0.7, 0.5, 0.3\}$ . The  
 frictionless case  $\mu = 0$  is included for visual comparison. Once again, the curves  
 660 below each structure in figure 14 show the pressure distribution on the contact  
 interfaces.

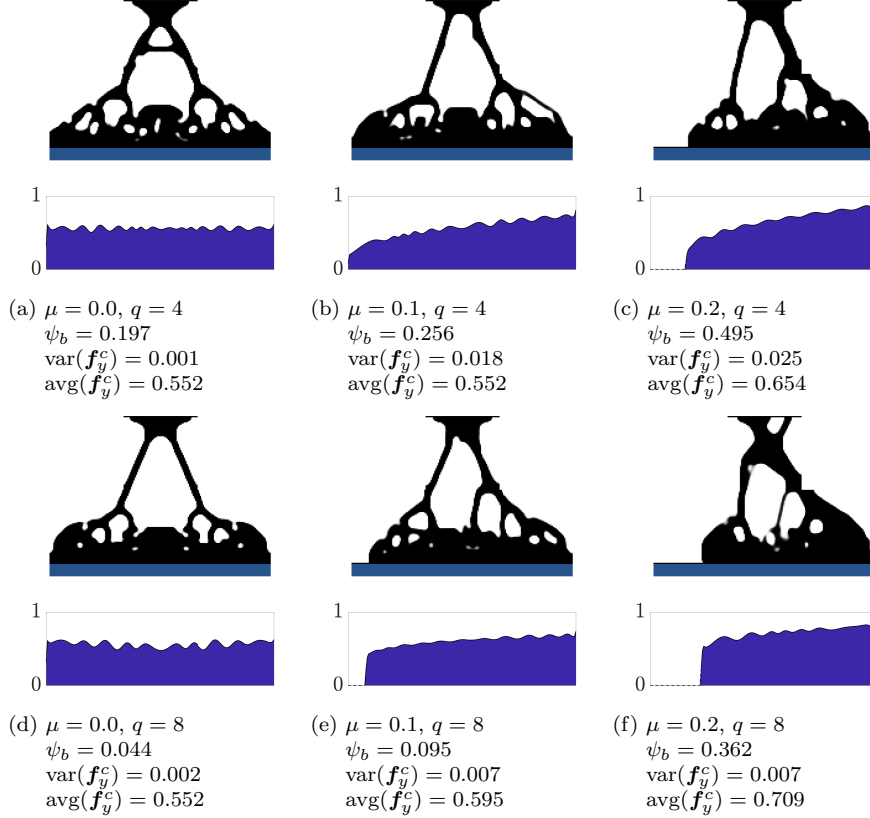


Figure 14: Optimized structures to test problem 3 for  $V^* = 0.3$  and  $\varphi^* = 4$  for different Coulomb friction coefficients and exponents  $q$ . The curve below each structure indicates the contact pressure along the lower edge of the domain.

For all examples in figure 14, the same trends are observed as in the previous section. Increasing  $q$  reduces the variation of the normal contact forces  $\mathbf{f}_y^c$ . It is also visible how the contact area decreases when  $q$  is increased. This leads to an increased average normal contact force.

665 For  $\mu = 0$ , small asymmetries are seen both for  $q = 4$  and  $q = 8$ , if the designs are closely inspected; these are assumed to be the result of numerical artifacts in the design sensitivities. However, the resulting designs are approximately symmetric as expected. For both cases of  $q = 4$  and  $q = 8$ , the optimizer utilizes the full potential contact area to lower the average pressure.

670 For  $\mu = 0.1$ , the effect of friction manifests itself as an asymmetry in the  
obtained designs for both values of  $q$ . However, the full potential contact area  
is utilized by the optimizer only for  $q = 4$ , to lower the average contact force,  
while this is not the case for  $q = 8$ . In the latter case, the optimizer reduces  
the actual contact area to avoid large variations in contact pressure. By further  
675 increasing  $\mu$  to 0.2 the obtained designs become even more asymmetric and for  
both values of  $q$ , the material distributions and the actual contact areas are  
heavily shifted towards the right-hand side of the domain.

## 6. Discussion and conclusions

This paper demonstrates how to combine methods for frictional contact me-  
680 chanics with modern density based topology optimization methods to achieve  
practically realizable designs optimized for either structural stiffness or favorable  
contact pressure distributions.

The first part of the paper was devoted to revisiting a compliance mini-  
mization with contact problem from the literature, for which we were able to  
685 demonstrate solid-void designs. The presented designs were obtained for dif-  
ferent volume constraints and load intensities, and three qualitatively different  
types of designs were obtained for this problem. Furthermore, we have added  
some complexity to this benchmark example by accounting for a more pro-  
nounced obstacle curvature, as well as by including friction up to  $\mu = 0.2$ . It  
690 was also demonstrated how the optimizer could disconnect the structure from  
its prescribed boundary conditions and regain support at the obstacle. The  
optimization was verified by cross checking the performance of the obtained  
designs.

The second part of the paper concerned optimization of contact pressure  
695 distribution over an a priori unknown contact area. To this end, a new objective  
function has been proposed, which aims at minimizing the average and the  
variation of the contact pressure. The proposed objective function includes a  
p-norm exponent  $q$  that controls the relative weighting of pressure variations  
compared to the average pressure in the optimization. For  $q = 1$  the objective  
700 function is simply the average contact pressure, while for  $q > 1$  variations of the  
pressure distribution are accounted for as well. Increasing  $q$  significantly evens  
out the pressure distribution but at the cost of an increased average pressure.  
To obtain meaningful results  $q$  should be larger than 1;  $q = 8$  has proven to be  
a good choice.

705 Complementing the pressure optimization problems with a compliance con-  
straint has proved crucial while the use of the robust formulation was neces-  
sary for achieving crisp solid-void designs. Excluding the compliance constraint  
makes the design problem ill conditioned as the minimization of the objective  
can be achieved by material removal that disconnects the contact surface from  
710 the external load. All in all, we have demonstrated different designs for different  
combinations of prescribed volume fractions, compliance constraints and values  
of the exponent  $q$ . The included numerical examples have also demonstrated

how the obtained designs are affected by including friction up to a friction coefficient of  $\mu = 0.2$ . As expected, including friction under sliding conditions, 715 resulted in asymmetric designs, that are drastically different from designs obtained from a frictionless model.

Regarding the limitations of the presented work, only contact of an elastic body against a rigid obstacle has been considered. Extending the proposed methods to include contact between two deformable bodies is rather straightforward and such a setting has already been presented, as previously mentioned, 720 in [27]. The proposed pressure objective has only been demonstrated in examples where contact is guaranteed but it is also applicable to cases where the contact area becomes zero during the design optimization. Moreover, a layer of prescribed solid along the potential contact area was included in all contact 725 pressure optimization examples. In principle, it is also possible though to avoid adding this prescribed solid layer, and consider all nodes, also internal ones, as potential contact nodes and let the optimizer determine the interface region. However, this is likely to result in designs with more grey material near the interface region or in the vicinity of the applied load.

The presented work utilizes the robust design methodology from [14] to ensure pure solid-void optimized designs with a prescribed minimum feature size. Although this approach comes at no extra computational cost for the minimum compliance problem, this is not the case for the proposed contact pressure objective function, where all three realizations are evaluated through finite element 730 analysis. Despite the three finite element problems are embarrassingly parallel in nature, one may argue that the extra cost should be avoided if possible. This could possibly be achieved using the geometric constraint from [43] which provides both length scale control as well as crisp designs without the need for additional finite element analysis. Alternatively, one could use the penalty approach from [15], although this approach does not ensure a minimum feature 740 size.

In conclusion, we would like to underline the potential practical aspects of optimizing contact pressure distributions by altering the design of an elastic structure in contrast to altering the initial gap between a structure and an 745 obstacle. A major limitation of the latter is the load sensitivity of the optimal initial gap shapes. Adding the possibility of affecting the contact pressure by changing the stiffness distribution in the underlying structure creates new opportunities.

## Acknowledgements

750 This work was funded by the Villum Foundation as a part of the InnoTop VILLUM investigator project. The authors have no competing interests.

## Appendix A. Partial derivatives of $C(\mathbf{f}_i^c, g, v, \mathbf{n})$

In order to calculate the Jacobian of the system of equations (9), the partial derivatives of the  $C$ -function are required. These are available for the general three-dimensional case in [30]. In the following, we include the simplified version of these derivatives, valid in the two-dimensional setting considered here.

It is convenient to start with stating the partial derivatives of the intermediate quantity  $\tau = \mu [\mathbf{f}_i^c \cdot \mathbf{n} + rg]_-$ , expressed as

$$\begin{aligned} \partial_{\mathbf{d}} P_{B(\mathbf{n}, \tau)}(\mathbf{d}) &= \begin{cases} \mathbf{T}_n & \text{if } \|\mathbf{T}_n \mathbf{d}\| \leq \tau \\ 0 & \text{otherwise} \end{cases} \\ \partial_{\tau} P_{B(\mathbf{n}, \tau)}(\mathbf{d}) &= \begin{cases} \frac{\mathbf{T}_n \mathbf{d}}{\|\mathbf{T}_n \mathbf{d}\|} & \text{if } 0 < \tau < \|\mathbf{T}_n \mathbf{d}\| \\ 0 & \text{otherwise} \end{cases} \\ \partial_{\mathbf{n}} P_{B(\mathbf{n}, \tau)}(\mathbf{d}) &= \begin{cases} 0 & \text{if } \tau \leq 0 \\ -\mathbf{d} \cdot \mathbf{n} \mathbf{T}_n - \mathbf{n} \otimes (\mathbf{T}_n \mathbf{d}) & \text{if } \|\mathbf{T}_n \mathbf{d}\| \leq \tau \\ -\frac{\tau}{\|\mathbf{T}_n \mathbf{d}\|} (\mathbf{n} \otimes (\mathbf{T}_n \mathbf{d})) & \text{otherwise} \end{cases} \end{aligned} \quad (29)$$

Finally, all partial derivatives of  $C(\mathbf{f}_i^c, g, v, \mathbf{n})$ , defined in Eq. (5), are obtained as

$$\begin{aligned} \partial_{\mathbf{f}_i^c} C(\mathbf{f}_i^c, g, v, \mathbf{n}) &= \mathbf{I} - \partial_{\mathbf{q}} \mathbf{P}_{B(\mathbf{n}, \tau)} - \partial_{\tau} \mathbf{P}_{B(\mathbf{n}, \tau)} \otimes \partial_{\mathbf{f}_i^c} \tau - H(-\mathbf{f}_i^c \cdot \mathbf{n} - rg) \mathbf{n} \otimes \mathbf{n} \\ \partial_g C(\mathbf{f}_i^c, g, v, \mathbf{n}) &= -\partial_{\tau} \mathbf{P}_{B(\mathbf{n}, \tau)} \partial_g \tau - H(-\mathbf{f}_i^c \cdot \mathbf{n} - rg) r \mathbf{n} \\ \partial_{\mathbf{n}} C(\mathbf{f}_i^c, g, v, \mathbf{n}) &= -\partial_{\mathbf{n}} \mathbf{P}_{B(\mathbf{n}, \tau)} - \partial_{\tau} \mathbf{P}_{B(\mathbf{n}, \tau)} \otimes \partial_{\mathbf{n}} \tau \\ &\quad - H(-\mathbf{f}_i^c \cdot \mathbf{n} - rg) (\mathbf{n} \otimes \mathbf{f}_i^c - (2\mathbf{f}_i^c \cdot \mathbf{n} + rg) \mathbf{n} \otimes \mathbf{n} + (\mathbf{f}_i^c \cdot \mathbf{n} + rg) \mathbf{I}) \\ \partial_v C(\mathbf{f}_i^c, g, v, \mathbf{n}) &= r \partial_{\mathbf{q}} \mathbf{P}_{B(\mathbf{n}, \tau)} \end{aligned} \quad (30)$$

## Appendix B

For completeness, below follows the full adjoint analysis used to obtain the sensitivities. First, we construct an augmented objective function  $\Psi(\mathbf{s}(\bar{\boldsymbol{\rho}}))$  by adding a zero-term to the original objective function, such that

$$\Psi(\mathbf{s}(\bar{\boldsymbol{\rho}}), \bar{\boldsymbol{\rho}}) = \psi(\mathbf{s}(\bar{\boldsymbol{\rho}})) + \boldsymbol{\lambda}^T \mathbf{R}(\mathbf{s}(\bar{\boldsymbol{\rho}}), \bar{\boldsymbol{\rho}}) \quad (31)$$

765 If we split the vector  $\mathbf{s}$  into two parts; and consider  $\mathbf{u}$  and  $\mathbf{f}_c$  separately, and ignore the function arguments for the sake of simplicity we can rewrite Eq. (31) into

$$\Psi = \psi + \boldsymbol{\lambda}^T \begin{pmatrix} \mathbf{R}_u \\ \mathbf{R}_c \end{pmatrix} \quad (32)$$

By differentiating Eq. (32) with respect to  $\bar{\boldsymbol{\rho}}$  we obtain

$$\underbrace{d_{\bar{\boldsymbol{\rho}}} \Psi}_{[1 \times ne]} = \underbrace{d_{\bar{\boldsymbol{\rho}}} \psi}_{[1 \times ne]} + \underbrace{\boldsymbol{\lambda}^T}_{[1 \times ndof]} \underbrace{\begin{pmatrix} d_{\bar{\boldsymbol{\rho}}} \mathbf{R}_u \\ d_{\bar{\boldsymbol{\rho}}} \mathbf{R}_c \end{pmatrix}}_{[ndof \times ne]} + \underbrace{\left\{ \underbrace{\begin{pmatrix} \partial_{\mathbf{u}} \psi \\ \partial_{\mathbf{c}} \psi \end{pmatrix}}_{[1 \times ndof]} + \underbrace{\boldsymbol{\lambda}^T}_{[1 \times ndof]} \underbrace{\begin{bmatrix} \partial_{\mathbf{u}} \mathbf{R}_u & \partial_{\mathbf{f}_c} \mathbf{R}_u \\ \partial_{\mathbf{u}} \mathbf{R}_c & \partial_{\mathbf{f}_c} \mathbf{R}_c \end{bmatrix}}_{[ndof \times ndof]} \right\}}_{[ndof \times ndof]} \underbrace{\begin{pmatrix} \partial_{\bar{\boldsymbol{\rho}}} \mathbf{u} \\ \partial_{\bar{\boldsymbol{\rho}}} \mathbf{f}_c \end{pmatrix}}_{[ndof \times ne]} \quad (33)$$

We refer to the matrix  $\begin{bmatrix} \partial_{\mathbf{u}} \mathbf{R}_u & \partial_{\mathbf{f}_c} \mathbf{R}_u \\ \partial_{\mathbf{u}} \mathbf{R}_c & \partial_{\mathbf{f}_c} \mathbf{R}_c \end{bmatrix}$  as  $\mathbf{J}$ , because this is the system Jacobian  
 770 which is also used in the Newton Raphson method to solve the state. To avoid evaluation of the gradients  $\partial_{\bar{\boldsymbol{\rho}}} \mathbf{u}$  and  $\partial_{\bar{\boldsymbol{\rho}}} \mathbf{f}_c$  we require the term within the curly braces to be zero. This requirement leads to the equation

$$\mathbf{J}^T \boldsymbol{\lambda} = - \begin{pmatrix} \partial_{\mathbf{u}} \psi \\ \partial_{\mathbf{f}_c} \psi \end{pmatrix} \quad (34)$$

Then Eq. (33) simplifies to

$$d_{\bar{\boldsymbol{\rho}}} \Psi = d_{\bar{\boldsymbol{\rho}}} \psi + \boldsymbol{\lambda}^T \begin{pmatrix} d_{\bar{\boldsymbol{\rho}}} \mathbf{R}_u \\ d_{\bar{\boldsymbol{\rho}}} \mathbf{R}_c \end{pmatrix} = d_{\bar{\boldsymbol{\rho}}} \psi + \boldsymbol{\lambda}^T \begin{pmatrix} \partial_{\bar{\boldsymbol{\rho}}_k} \mathbf{K} \mathbf{u} \\ \mathbf{0} \end{pmatrix} \quad (35)$$

By considering Eq. (9), it is clear that of the two gradients  $d_{\bar{\boldsymbol{\rho}}} \mathbf{R}_u$  and  $d_{\bar{\boldsymbol{\rho}}} \mathbf{R}_c$ ,  
 775 only  $d_{\bar{\boldsymbol{\rho}}} \mathbf{R}_u$  has an explicit dependence on the design variables  $\bar{\boldsymbol{\rho}}$ , such that  $d_{\bar{\boldsymbol{\rho}}} \mathbf{R}_u = \partial_{\bar{\boldsymbol{\rho}}_k} \mathbf{K} \mathbf{u}$  and  $d_{\bar{\boldsymbol{\rho}}} \mathbf{R}_c = \mathbf{0}$ .

### Compliance optimization

In the case of compliance optimization of linear elastic structures with unilateral contact the following expressions are used to obtain the design sensitivities

780

$$\mathbf{J}^T \boldsymbol{\lambda} = - \begin{pmatrix} 2\mathbf{K} \mathbf{u} \\ \mathbf{0} \end{pmatrix} \quad \text{and} \quad \partial_{\bar{\boldsymbol{\rho}}_{k,i}} \phi_k = \mathbf{u}^T \partial_{\bar{\boldsymbol{\rho}}_{k,i}} \mathbf{K} \mathbf{u} + \boldsymbol{\lambda}^T \begin{pmatrix} \partial_{\bar{\boldsymbol{\rho}}_{k,i}} \mathbf{K} \mathbf{u} \\ \mathbf{0} \end{pmatrix} \quad (36)$$

*Pressure optimization*

For an objective function defined as

$$\psi_k(\mathbf{s}) = \frac{a(\mathbf{s})}{b(\mathbf{s})} = \frac{\sum_i a_i p_i^q}{\sum_i a_i H(p_i) + \left[1 - H\left(\sum_i a_i p_i\right)\right] \epsilon} \quad (37)$$

The gradient  $\partial_{\mathbf{f}_c} \psi_k$  become

$$\partial_{\mathbf{f}_c} \psi_k = \frac{b \partial_{\mathbf{s}} a - a \partial_{\mathbf{s}} b}{b^2} \quad (38)$$

where

$$\begin{aligned} \partial_{\mathbf{s}} a &= \mathbf{p}^{q-1} \mathbf{q} \\ \partial_{\mathbf{s}} b &= \sum_{\text{assembly}}^i a_i H'(p_i) - \epsilon a_i H'\left(\sum_i a_i p_i\right) \end{aligned} \quad (39)$$

785 Such that the adjoint problem for the objective function is

$$\mathbf{J}^T \boldsymbol{\lambda}_1 = - \begin{pmatrix} \mathbf{0} \\ \partial_{\mathbf{f}_c} \psi_k \end{pmatrix} \quad \text{and} \quad \partial_{\bar{\rho}_{k,i}} \psi_k = \boldsymbol{\lambda}_1^T \begin{pmatrix} \partial_{\bar{\rho}_k} \mathbf{K} \mathbf{u} \\ \mathbf{0} \end{pmatrix} \quad (40)$$

and the adjoint problem for the compliance constraint is

$$\mathbf{J}^T \boldsymbol{\lambda}_2 = - \begin{pmatrix} \mathbf{f}^{ext} \\ \mathbf{0} \end{pmatrix} \quad \text{and} \quad \partial_{\bar{\rho}_{e,i}} \varphi_e = \boldsymbol{\lambda}_2^T \begin{pmatrix} \partial_{\bar{\rho}_e} \mathbf{K} \mathbf{u} \\ \mathbf{0} \end{pmatrix} \quad (41)$$

- [1] M. P. Bendsøe, Optimal shape design as a material distribution problem, *Structural optimization* 1 (4) (1989) 193–202.
- 790 [2] N. Aage, E. Andreassen, B. S. Lazarov, O. Sigmund, Giga-voxel computational morphogenesis for structural design, *Nature* 550 (7674) (2017) 84.
- [3] C. S. Andreasen, A. R. Gersborg, O. Sigmund, Topology optimization of microfluidic mixers, *International Journal for Numerical Methods in Fluids* 61 (5) (2009) 498–513.
- 795 [4] N. Aage, T. H. Poulsen, A. Gersborg-Hansen, O. Sigmund, Topology optimization of large scale stokes flow problems, *Structural and Multidisciplinary Optimization* 35 (2) (2008) 175–180.
- [5] R. E. Christiansen, O. Sigmund, Designing meta material slabs exhibiting negative refraction using topology optimization, *Structural and Multidisciplinary Optimization* 54 (3) (2016) 469–482.
- 800 [6] M. B. Dühring, J. S. Jensen, O. Sigmund, Acoustic design by topology optimization, *Journal of sound and vibration* 317 (3-5) (2008) 557–575.
- [7] D. Hilding, A. Klarbring, J.-S. Pang, Minimization of maximum unilateral force, *Computer Methods in Applied Mechanics and Engineering* 177 (3-4) (1999) 215–234.
- 805 [8] N. Strömberg, A. Klarbring, Minimization of compliance of a linear elastic structure with contact constraints by using sequential linear programming and newtons method, in: *The Proceedings of the 7th International ASMOUK/ISSMO International Conference on Engineering Design Optimization*, Bath, UK, 2008.
- 810 [9] N. Strömberg, A. Klarbring, Topology Optimization of Structures with Contact Constraints by using a Smooth Formulation and a Nested Approach, 8th World Congr. Struct. Multidiscip. Optim. 1 (2009) 1–8.
- [10] D. Hilding, A heuristic smoothing procedure for avoiding local optima in optimization of structures subject to unilateral constraints, *Structural and multidisciplinary optimization* 20 (1) (2000) 29–36.
- 815 [11] N. Strömberg, Topology optimization of structures with manufacturing and unilateral contact constraints by minimizing an adjustable compliance–volume product, *Structural and Multidisciplinary Optimization* 42 (3) (2010) 341–350.
- 820 [12] N. Strömberg, A. Klarbring, Topology optimization of structures in unilateral contact, *Structural and Multidisciplinary Optimization* 41 (1) (2010) 57–64.
- [13] N. Strömberg, The influence of sliding friction on optimal topologies, in: *Recent Advances in Contact Mechanics*, Springer, 2013, pp. 327–336.

- 825 [14] F. Wang, B. S. Lazarov, O. Sigmund, On projection methods, convergence and robust formulations in topology optimization, *Structural and Multidisciplinary Optimization* 43 (6) (2011) 767–784.
- [15] T. Borrvall, J. Petersson, Topology optimization using regularized intermediate density control, *Computer Methods in Applied Mechanics and Engineering* 190 (37-38) (2001) 4911–4928. doi:10.1016/S0045-7825(00)00356-X.
- 830 [16] Achieving minimum length scale in topology optimization using nodal design variables and projection functions, *International Journal for Numerical Methods in Engineering* 61 (September 2003) (2004) 238–254. doi:10.1002/nme.1064.
- 835 [17] A. Klarbring, On the problem of optimizing contact force distributions, *Journal of optimization theory and applications* 74 (1) (1992) 131–150.
- [18] J. Zowe, M. Kočvara, M. P. Bendsøe, Free material optimization via mathematical programming, *Mathematical programming* 79 (1-3) (1997) 445–466.
- 840 [19] M. Patriksson, J. Petersson, A subgradient method for contact structural optimization, in: *Complementarity and Variational Problems— State of the Art, Proceedings of the International Conference on Complementarity Problems (ICCP-95)*, MC Ferris and J.-S. Pang (eds.), SIAM, Philadelphia, PA, 1997, pp. 295–314.
- 845 [20] J. Petersson, M. Patriksson, Topology optimization of sheets in contact by a subgradient method, *International journal for numerical methods in engineering* 40 (7) (1997) 1295–1321.
- [21] M. Kočvara, M. Zibulevsky, J. Zowe, Mechanical design problems with unilateral contact, *ESAIM: Mathematical Modelling and Numerical Analysis* 32 (3) (1998) 255–281.
- 850 [22] D. Hilding, A. Klarbring, J. Petersson, Optimization of structures in unilateral contact, *Applied Mechanics Reviews* 52 (4) (1999) 139–160.
- [23] B. Desmorat, Structural rigidity optimization with frictionless unilateral contact, *International Journal of Solids and Structures* 44 (3) (2007) 1132–1144.
- 855 [24] A. Andrade-Campos, A. Ramos, J. A. Simões, A model of bone adaptation as a topology optimization process with contact, *Journal of Biomedical Science and Engineering* 5 (05) (2012) 229.
- 860 [25] Y. Luo, M. Ll, Z. Kang, Topology optimization of hyperelastic structures with frictionless contact supports, *International Journal of Solids and Structures* 81 (2016) 373–382.

- [26] D. Hilding, A. Klarbring, Optimization of structures in frictional contact, *Computer Methods in Applied Mechanics and Engineering* 205 (2012) 83–90.
- [27] M. Lawry, K. Maute, Level set topology optimization of problems with sliding contact interfaces, *Structural and Multidisciplinary Optimization* 52 (6) (2015) 1107–1119.
- [28] A. Klarbring, J. Petersson, M. Rönqvist, Truss topology optimization including unilateral contact, *Journal of optimization theory and applications* 87 (1) (1995) 1–31.
- [29] P. Alart, A. Curnier, A mixed formulation for frictional contact problems prone to newton like solution methods, *Computer methods in applied mechanics and engineering* 92 (3) (1991) 353–375.
- [30] K. Poullos, Y. Renard, An unconstrained integral approximation of large sliding frictional contact between deformable solids, *Computers & Structures* 153 (2015) 75–90.
- [31] Y. Renard, Generalized newtons methods for the approximation and resolution of frictional contact problems in elasticity, *Computer Methods in Applied Mechanics and Engineering* 256 (2013) 38–55.
- [32] O. Sigmund, Design of material structures using topology optimization, Ph.D. thesis, Technical University of Denmark Denmark (1994).
- [33] T. Buhl, C. B. Pedersen, O. Sigmund, Stiffness design of geometrically nonlinear structures using topology optimization, *Structural and Multidisciplinary Optimization* 19 (2) (2000) 93–104.
- [34] O. Sigmund, A 99 line topology optimization code written in matlab, *Structural and multidisciplinary optimization* 21 (2) (2001) 120–127.
- [35] J. P. Groen, O. Sigmund, Homogenization-based topology optimization for high-resolution manufacturable microstructures, *International Journal for Numerical Methods in Engineering*.
- [36] B. Bourdin, Filters in topology optimization, *International Journal for Numerical Methods in Engineering* 50 (9) (2001) 2143–2158.
- [37] M. P. Bendsøe, O. Sigmund, Material interpolation schemes in topology optimization, *Archive of applied mechanics* 69 (9-10) (1999) 635–654.
- [38] O. Sigmund, Manufacturing tolerant topology optimization, *Acta Mechanica Sinica* 25 (2) (2009) 227–239.
- [39] O. Sigmund, Morphology-based black and white filters for topology optimization, *Structural and Multidisciplinary Optimization* 33 (4-5) (2007) 401–424.

- 900 [40] K. Svanberg, The method of moving asymptotes - A new method for structural optimization, *International journal for numerical methods in engineering* 24 (2) (1987) 359–373.
- [41] J. Petersson, *Optimization of structures in unilateral contact*, Univ., 1995.
- 905 [42] J. K. Guest, A. Asadpoure, S.-H. Ha, Eliminating beta-continuation from heaviside projection and density filter algorithms, *Structural and Multidisciplinary Optimization* 44 (4) (2011) 443–453.
- [43] M. Zhou, B. S. Lazarov, F. Wang, O. Sigmund, Minimum length scale in topology optimization by geometric constraints, *Computer Methods in Applied Mechanics and Engineering* 293 (2015) 266–282. doi:10.1016/j.cma.2015.05.003.
- 910